Contents lists available at ScienceDirect

Applied Clay Science

journal homepage: www.elsevier.com

Research paper

Ni-bearing phyllosilicates ("garnierites"): New insights from thermal analysis, μRaman and IR spectroscopy

Cristina Villanova-de-Benavent [a, b, *], Tariq Jawhari [c], Josep Roqué-Rosell [a], Salvador Galí [a], Joaquín A. Proenza [a]

[a] Departament de Mineralogia, Petrologia i Geologia Aplicada, Facultat de Geologia, Universitat de Barcelona, Martí i Franquès s/n, 08028 Barcelona, Spain
[b] School of Environmental and Technology (SET), University of Brighton, Cockroft Building, Lewes Road, BN4 2GJ Brighton, United Kingdom
[c] Centres Científics i Tecnològics, Universitat de Barcelona, Lluís Solé i Sabarís, 1-3, 08028 Barcelona, Spain

ARTICLE INFO

Keywords:
Garnierite
Ni-Mg-phyllosilicates
Raman spectroscopy
FTIR
DTA-TG
Dominican Republic

ABSTRACT

Ni-Mg-phyllosilicates, so-called "garnierites", are significant Ni ores in Ni-laterite deposits worldwide. In addition, they are the natural analogues of synthetic catalysts involving Ni and phyllosilicate substrates used in reactions for the remediation of greenhouse gases. However, the nomenclature, classification and characterisation of Ni-Mg-phyllosilicates is a long-lasting problem, because of their fine-grained nature, poor crystallinity and frequent occurrence as intimate mixtures. This work presents and discusses DTA-TG, Raman and FTIR spectroscopy data of a series of well characterised, naturally occurring Ni-Mg-phyllosilicate samples with a variety of mineral compositions (including serpentine-dominated, talc-dominated and sepiolite-falcondoite, with various Ni contents). The results are compared to data obtained from crystalline, 1:1 and 2:1 Mg-phyllosilicates and from the literature. DTA-TG confirmed that the talc-like fraction in garnierite mixtures belongs to the kerolite-pimelite series. The different garnierite types analysed are distinguishable from their Raman and FTIR spectra, and the serpentine, talc and sepiolite components could be identified (e.g. by Raman bands at ~690 cm^{-1}, ~670 cm^{-1} and ~200 cm^{-1}, respectively). Knowledge of Raman and FTIR vibrations of garnierites with constrained structure and composition is paramount in order to effectively characterise these phyllosilicates, and can be applied to mineral identification in ore exploration and processing, and after synthesis for nanotechnology purposes.

1. Introduction

Ni-Mg-phyllosilicates, often grouped under the term "garnierites", are important Ni ore minerals in weathering profiles developed on ultramafic rocks (e.g. Golightly, 1981, 2010; Freyssinet et al., 2005). This group of minerals had been extensively studied during the 1960s to early 1980s (Caillère, 1965; Faust, 1966; Brindley and Hang, 1973; Brindley, 1978) and gained interest recently (Wells et al., 2009; Villanova-de-Benavent et al., 2014, 2016; Cathelineau et al., 2016; Fritsch et al., 2016; Roqué-Rosell et al., 2017; Čermáková et al., 2017). The problem with the identification of the garnierite minerals deals with their poorly crystalline, fine grained nature and their frequent occurrence as mixtures of serpentine, talc, sepiolite, chlorite and/or smectite (e.g. Brindley and Hang, 1973). Apart from their significance as Ni ores, garnierites are in fact the natural analogues of widely described synthetic catalysts involving Ni and phyllosilicate substrates (Kawi and Zao, 1999; Melo et al., 2008; McDonald et al., 2009; Bloise et al., 2010; Kong et al., 2015), with applications such as the remediation of greenhouse gases (e.g. Sivaiah et al., 2011; Bian et al., 2015). Even more so, some natural garnierites have been considered as plausible catalysts (Jacobs et al., 1980; Linares et al., 2014) because the Ni concentration is similar to that of certain commercial catalysts (Topsoe et al., 1996).

Differential thermal analysis coupled with thermogravimetry (DTA-TG) has been historically used to identify most phyllosilicate groups (Caillère and Hénin, 1957a, 1957b, 1957c) and is essential to determine the amount and the location of water in their structures. Actually, it has been proven very useful to distinguish among the serpentine group minerals (Viti, 2010). Some authors studied the thermal behaviour of certain garnierite types, with a limited number of samples (Caillère, 1965; Hang and Brindley, 1973; Springer, 1976; Tauler et al.,

* Corresponding author at: School of Environmental and Technology (SET), University of Brighton, Cockroft Building, Lewes Road, BN4 2GJ Brighton, United Kingdom.
Email address: cvillanovadb@gmail.com (C. Villanova-de-Benavent)

https://doi.org/10.1016/j.clay.2019.03.036
Received 3 July 2018; Received in revised form 28 March 2019; Accepted 31 March 2019
Available online xxx
0169-1317/

2009; Bunjaku et al., 2011; Sufriadin et al., 2012), but a comparative study including different mineral compositions is needed, as detailed studies are scarce (Fritsch et al., 2016).

Micro-Raman spectroscopy represents an easy, trustworthy and non-destructive method that can be used to distinguish phyllosilicate minerals in situ, even when samples are very fine grained, consist of intimate mixtures at the nanometre scale and/or are poorly crystalline. In particular, serpentine group minerals (antigorite, lizardite and chrysotile) are easily identified by this technique, as each of them displays characteristic Raman bands (Rinaudo et al., 2003). In addition, a very detailed, recent study on the so-called talc-like, kerolite-pimelite series provides valuable hints on the variation of the Raman effects with Ni content (Cathelineau et al., 2014, 2015). However, available mineral databases of micro-Raman spectra lack trustworthy references of most garnierite minerals.

Complementary to DTA-TG and Raman spectroscopy, infrared spectroscopy contributes to a better understanding of the structure of Mg—Ni— phyllosilicates (Brindley and Wan, 1975; Brindley et al., 1979), but most studies focussed on a single mineral species or series (Ishida, 1990; Kloprogge et al., 2000; Yeniyol, 2014), or analysed synthetic Ni-phyllosilicates (Dumas et al., 2013; Baron and Petit, 2016; Blanchard et al., 2018).

The present work provides and discusses detailed DTA-TG, Raman and IR spectroscopy data from garnierite samples made of various proportions of serpentine- and talc-like minerals, and sepiolite-falcondoite, with well constrained mineral compositions. The results are compared with data obtained from crystalline 1:1 and 2:1 Mg-phyllosilicates (serpentine, talc and sepiolite) and with data from the literature. The aims are to demonstrate the viability of these techniques to provide a reliable and easy identification of the poorly understood garnierite mixtures, and to shed light on the effect of the mineral chemistry (in terms of Ni, Si and water contents) on the thermal and spectroscopic study of these minerals. A better knowledge on the thermal behaviour and the Raman and FTIR response of Ni-Mg-phyllosilicates could be used to better constrain the mineral composition of the material derived to the smelting furnace during mineral processing, and to help unravel the stability and properties of similar synthetic phyllosilicates for their specific nanotechnological purposes.

2. Materials and methods

2.1. Samples

For the present study, eight garnierite samples from the Falcondo Ni-laterite mining district in central Dominican Republic (Fig. 1a) were selected as the most representative of the five types described in Villanova-de-Benavent et al. (2014, 2016) and Roqué-Rosell et al. (2017) in terms of their structure and composition determined by powder X-ray diffraction (XRD), electron microprobe (EMP) and transmission electron microscopy (TEM) (Table 1): a) types I and II (dominated by serpentine-like minerals); b) types III and IV (mixed serpentine- and talc-like minerals); and c) type V (sepiolite-falcondoite).

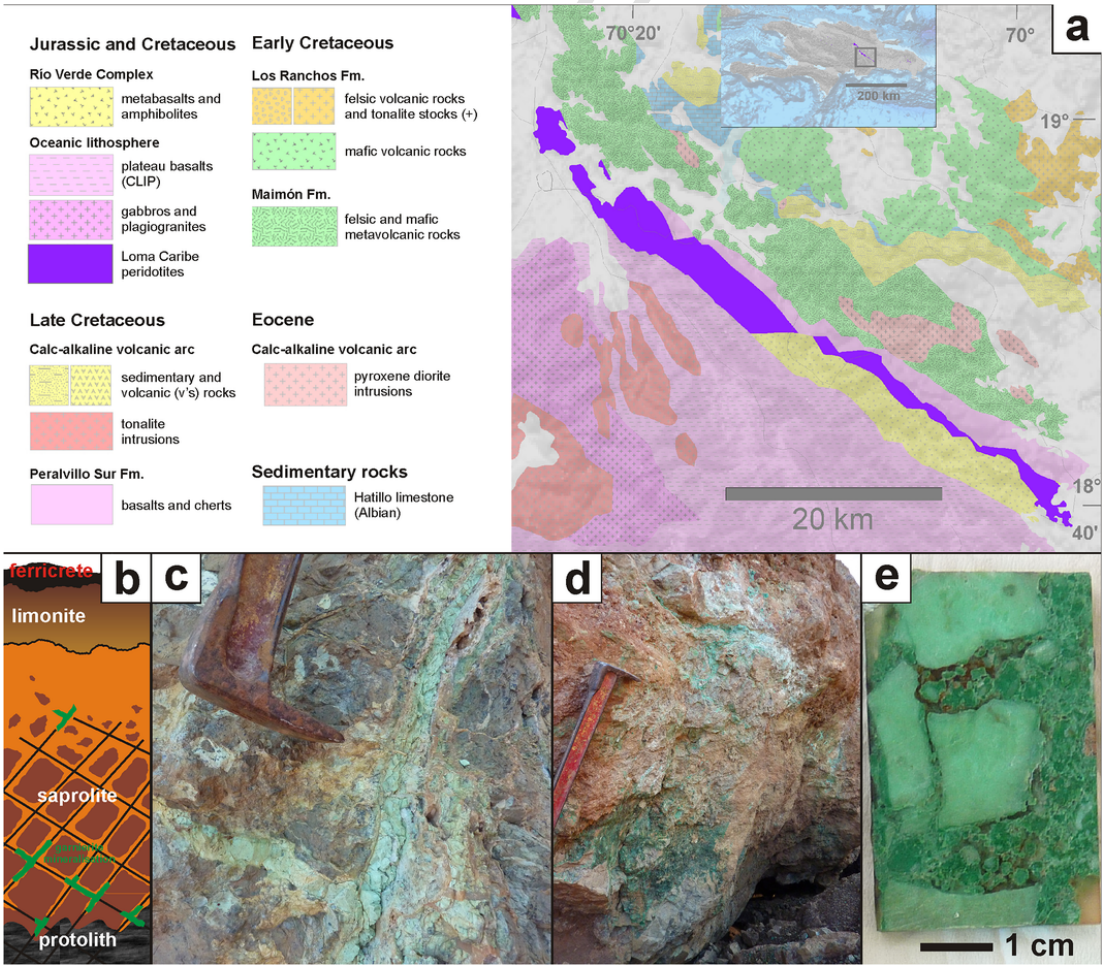

Fig. 1. Geological setting and mode of occurrence in the field of garnierite mineralisations in the Falcondo mining district: (a) geological map of the Ni-laterite deposit formed by weathering of the Loma Caribe peridotite (modified from Nelson et al., 2015); (b) schematic Ni-laterite profile in the study area; (c) garnierite veins, (d) coatings and (e) breccias.

Table 1
List of the samples analysed by DTA-TG, Raman spectroscopy and FTIR for this study, including the mineralogy (obtained by powder XRD), the average structural formulae (analysed by EMP, number of analyses averaged in brackets), the calculated talc fraction of the garnierite mixtures (Xtalc) and the provenance of the samples (n.a. = not analysed, < d.l. = below detection limit). $*Xtalc = 1.5 \times \frac{\sum \text{tetra}}{\sum \text{octa}} - 1$.

	Sample	Mineralogy (XRD)	Structural formula (EMP)	NiO (wt.%)	Xtalc*	Locality
lizardite	LIZ-1	lizardite (7.29 Å)	*n.a.*	*n.a.*	-	Cornwall (United Kingdom)
lizardite	LIZ-2	lizardite (7.26 Å)	$Mg_{2.74}Al_{0.16}Fe_{0.15}Si_{1.90}O_5(OH)_4$ [15]	0.02-0.06	-	Elba Island (Italy)
chrysotile	CRIS	chrysotile (7.30 Å)	$Mg_{2.79}Fe_{0.11}Mn_{0.01}Si_{2.02}O_5(OH)_4$ [3]	< 0.01	-	Huelva (Spain)
talc	TLC	talc (9.35 Å)	$Mg_{2.94}Al_{0.01}Fe_{0.01}Si_{4.01}O_{10}(OH)_2$ [7]	< 0.02	-	León (Spain)
sepiolite	SEP	sepiolite (11.89 Å)	$Mg_{3.82}Fe_{0.04}Al_{0.01}Si_{6.04}O_{15}(OH)_2{\cdot}6H_2O$ [3]	< d.l.	-	Setcases (Spain)
Type I	09GAR-2	serpentine (7.26-7.32 Å)	$(Mg_{2.34}Ni_{0.48}Fe_{0.15})Si_{2.48}O_{5.27}(OH)_{3.49}{\cdot}0.26H_2O$ [16]	3.19-14.58	0.26	Falcondo (Dominican Republic)
Type II	LC-100	serpentine (7.30 Å) + talc-like (10.20-10.54 Å)	$(Mg_{2.09}Ni_{0.87}Fe_{0.05})(Si_{2.53}Al_{0.09})O_{6.53}(OH)_{3.39}{\cdot}0.31H_2O$ [66]	3.77-26.62	0.31	Falcondo (Dominican Republic)
Type III	GAR-2	serpentine (7.40 Å) + talc-like (10.56 Å)	$(Ni_{2.42}Mg_{0.58}Fe_{0.01})Si_{2.71}O_{6.81}(OH)_{3.28}{\cdot}0.36H_2O$ [4]	42.90-45.24	0.36	Falcondo (Dominican Republic)
Type IV	GAR-6	talc-like (9.94-10.14 Å ± 7.34 Å)	$(Ni_{1.90}Mg_{1.10})(Si_{3.61}Al_{0.01})O_{9.06}(OH)_{2.40}{\cdot}0.81H_2O$ [17]	24.26-38.91	0.81	Falcondo (Dominican Republic)
	LC-100	talc-like (9.94-10.14 Å ± 7.34 Å)	$(Ni_{1.95}Mg_{1.04})Si_{3.69}O_{9.24}(OH)_{2.30}{\cdot}0.85H_2O$ [109]	18.37-44.39	0.85	Falcondo (Dominican Republic)
Type Va - Ni-sepiolite	FALC-4	sepiolite (12.07 Å)	$Mg_{7.02}Ni_{0.51}Fe_{0.12}Si_{12.11}Al_{0.02}O_{15}(OH)_2{\cdot}6H_2O$ [16]	2.06-3.53	-	Falcondo (Dominican Republic)
Type Vb - falcondoite	FALC-3	sepiolite (12.15 Å)	$Ni_{4.43}Mg_{3.42}Fe_{0.01}Si_{11.89}Al_{0.12}O_{15}(OH)_2{\cdot}6H_2O$ [3]	18.26-26.82	-	Falcondo (Dominican Republic)

The garnierite mineralisations exposed in the Ni-laterite mining pits are found mainly within the lowermost part of the saprolite (lower, serpentine-rich horizon), and less frequently in unweathered serpentinised peridotite (bedrock) at the base of the profile and in the upper saprolite horizon (Fig. 1b), occurring mainly as veins in fractures (Fig. 1c), or coatings on fault surfaces (Fig. 1d), and as clasts and/or cements in breccias (Fig. 1e).

Type I garnierite is yellowish pale green (Fig. 2a) in colour and consists of serpentine according to powder XRD (Table 1, Villanova-de-Benavent et al., 2014); but TEM investigations reveal the presence of thin talc-like fibres (Villanova-de-Benavent et al., 2016). This garnierite type has the lowest Ni contents in Falcondo garnierites (3.19–14.58 wt% NiO in the analysed sample) (Fig. 2l); and is the only with remarkable Fe content (1.66–5.35 wt% Fe_2O_3), whereas Fe is mostly below detection limit in the other garnierite types (Table 1). Type II is apple green and often occurs as coatings on angular saprolite fragments (Fig. 2b). It is characterised by a very intense and sharp reflection at ~7.30 Å, and a lower, broader reflection at ~10 Å, corresponding to the basal spacings of serpentine group minerals and talc, respectively (Table 1). This suggests that the sample consists of a serpentine-like phase with talc-like impurities, as confirmed by TEM (Villanova-de-Benavent et al., 2016) (Fig. 2b). The Ni content is higher than in type I, between 3.77 and 26.62 wt% NiO in the sample selected for this study (Fig. 2l, Table 1). Type III garnierite displays an intense green colour with a characteristic dull to greasy lustre. It occurs as coatings on other garnierites and cements in breccias (Fig. 2c). It has two reflections with similar intensities around 7.30 Å and 10 Å, indicating a mixture of serpentine- and talc-like phases at the nanometre scale (Table 1). Type III garnierites contain the highest Ni content of the Falcondo garnierites, from 42.90 to 45.24 wt% NiO in the selected sample (Fig. 2l, Table 1). Type IV is bluish green, and forms thin coatings and cements in breccias, is often overgrown by microcrystalline quartz that fills porosity (Fig. 2a, b and d). Type IV garnierite only shows a broad reflection at ~10 Å suggesting that it consists of a talc-like phase (Table 1). It yields a wide range of Ni compositions: between 18.37 and 44.39 wt% NiO in the samples selected for this study (Fig. 2l, Table 1). Its most characteristic feature is the appearance as banded botryoidal aggregates observed under the optical microscope (Villanova-de-Benavent et al., 2014). Its texture and mineral chemistry is similar to those of the kerolite-pimelite from New Caledonia described and analysed by Wells et al., 2009, Fig. 7) and Cathelineau et al. (2016). Type V garnierite forms white (Ni-sepiolite, Fig. 2e) to pale green (falcondoite, Fig. 2f) compact sets of schistose, friable, soft material. As type IV garnierites, sepiolite-falcondoite have various Ni concentrations, between 2.06 and 26.82 wt% NiO in the selected samples (Fig. 2l, Table 1). Different types of garnierite may coexist in the same sample (Fig. 2a and b), however, it is important to point out that sepiolite-falcondoite have never been observed in contact with garnierite types I to IV (serpentine- and talc-like garnierite mixtures) in the study area, unlike in the case of New Caledonia (Fritsch et al., 2016).

The study is complemented with samples of crystalline 1:1 and 2:1 Mg-phyllosilicates from other localities, in order to detect differences in thermal behaviour and Raman and IR response between Ni-bearing and their corresponding Mg end members; including lizardite from Lizard, Cornwall (lizardite type locality, United Kingdom; Fig. 2g) and Elba Island (Italy; Fig. 2h), and chrysotile, talc and sepiolite (from Huelva, León and Setcases, respectively, in Spain; Fig. 2i–k) (Table 1).

2.2. Differential thermal analysis and thermogravimetry (DTA-TG)

The same powders studied by XRD were later analysed by DTA-TG (Netzsch STA 409C/CD) in the Departament de Mineralogia, Petrologia i Geologia Aplicada, Facultat de Ciències de la Terra, of the Universitat de Barcelona. DTA was acquired from 50 mg of each garnierite type and the crystalline 1:1 and 2:1 Mg-phyllosilicate reference samples using an alumina crucible, from 25 to 1000 °C at 10 °C/min, under a dry air atmosphere with a flow rate of 80 mL/min. The software Netzsch Proteus Analysis® was used to calculate the loss of water for each step in the TG diagrams, and to obtain the temperatures of the endothermic and exotermic peaks in the DTA diagrams (the maxima and minima of the curves, respectively).

2.3. Micro-raman spectroscopy

Raman spectra were obtained on polished thin sections with a HORIBA JobinYvon LabRam HR 800 dispersive spectrometer equipped with an Olympus BXFM optical microscope in the Centres Científics i Tecnològics of the Universitat de Barcelona (CCiT-UB). Different laser wavelengths were tested in order to obtain the best possible spectra avoiding fluorescence related to crystalline defects and fluorescence emitting centres: 325 nm (near ultraviolet), 532 nm (green), 785 nm (red) and 1064 nm (near infrared). Best results were obtained with the 1064 nm laser, and spectra using the 532 nm wavelength are also displayed, for comparison (despite strong fluorescence effects), and to show the high frequency region ($> 3300\ cm^{-1}$). Non polarized Raman spectra were obtained in the backscattering confocal geometry, with a 50× objective for the NIR measurements (beam size around 2 μm) and 100× objective (beam size around 1 μm) for visible Raman analysis, with 10 measurement repetitions for 60 s each. An InGaAs detector cooled at and −110 °C was used for the Raman measurements obtained in the NIR excitation laser, whereas for the visible experiment a CCD detector cooled at −40 °C was utilized. The instrument was calibrated by regularly recording a silicon reference and checking the position of the silicon band at $\sim 520\ cm^{-1}$. The micro-Raman data were processed using the LabSpec® software (Jobin Yvon). The final spectra were produced by subtracting the fluorescence signal.

A micro-Raman map was obtained on a selected region of interest containing saprolite fragments and two different types of garnierites. This map allows the observation of the distribution of the different species in the analysed area by their respective characteristic Raman spectrum. This map was performed using a WITec alpha300RA + Con-

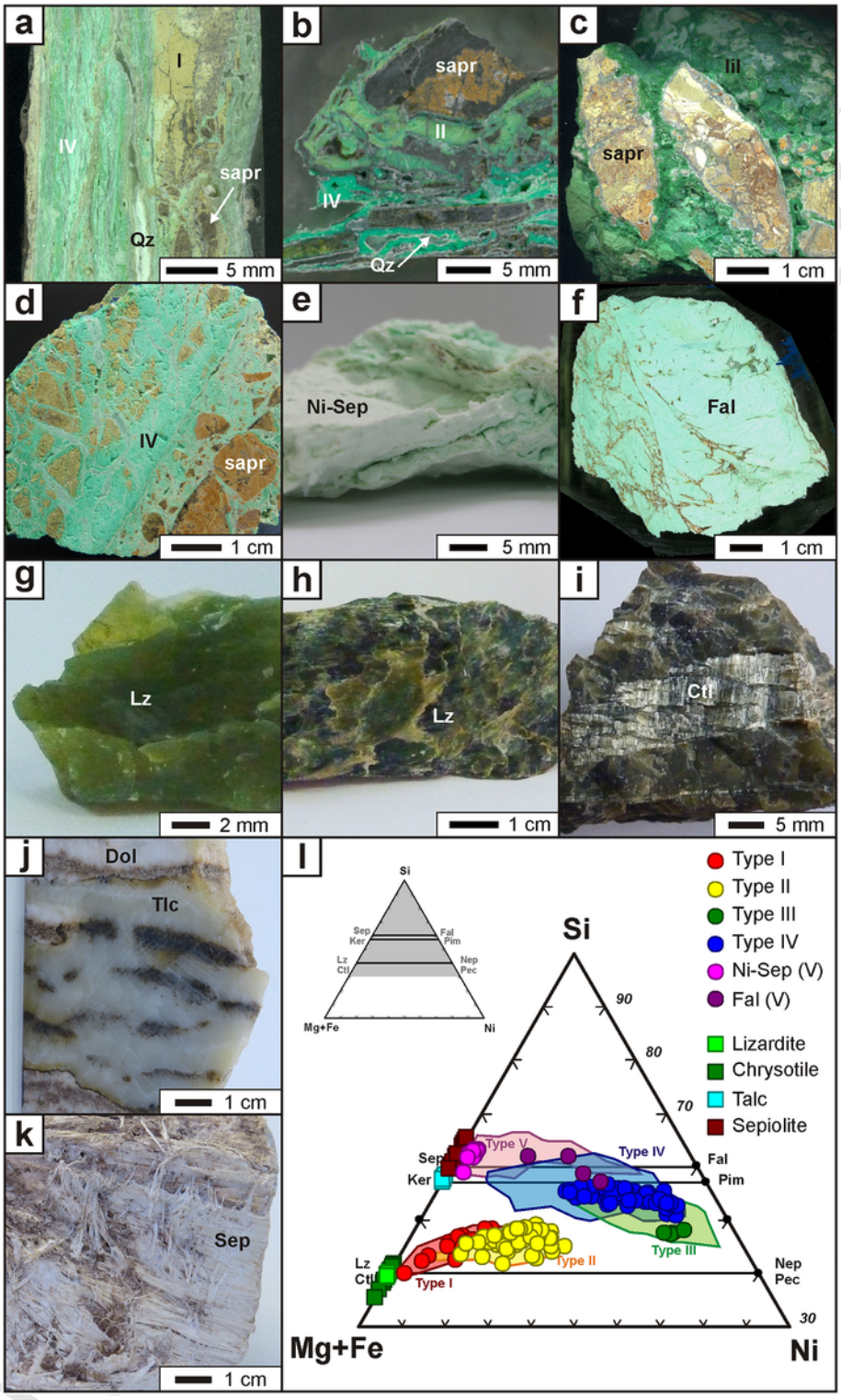

Fig. 2. Hand specimen pictures (a-k) and mineral composition (l) of the studied Ni—Mg phyllosilicates: a) type I garnierite (sample 09GAR-2), b) type II garnierite (LC-100A), c) type III garnierite (GAR-2), d) type IV garnierite (GAR-6), e) type Va Ni-sepiolite (FALC-4), f) type Vb falcondoite (FALC-3), g) lizardite (LIZ-1, from Cornwall), h) lizardite (LIZ-2, from Elba island), i) chrysotile (CRIS, from Huelva), j) talc (TLC, from León), k) sepiolite (SEP, from Setcases). Legend: I–IV = garnierite types I–IV, sapr = saprolite fragment, Qz = quartz, Ni-Sep = Ni-sepiolite, Fal = falcondoite, Lz = lizardite, Ctl = chrysotile, Tlc = talc, Dol = dolomite, Sep = sepiolite. The ternary diagram (l) includes EMP analyses of the samples 09GAR-2 (I), LC-100 (II and IV), GAR-2 (III), GAR-6 (IV), FALC-4 (Ni-sepiolite) and FALC-3 (falcondoite), fields from Villanova-de-Benavent et al. (2014). Legend: Ker = kerolite, Pim = pimelite, Nep = népouite, Pec = pecoraite.

focal Raman Imaging Microcoscope, with a 532 nm laser (CCiT-UB). The size of the analysed area is 6750 × 1000 μm, with 100 scanned lines and 675 analysed points per image (i.e. Raman spectrum is recorded every 10 μm), and 0.3 s of integration time (202.5 s per line). The map was obtained after scanning the area, applying a cluster analysis to the confocal Raman image, which allow to group the Raman spectra according to their similarities in the range 150–750 cm^{-1} (where serpentine and talc phases present more differences in band po-

sition and intensity), and merging the areas into one single image in which the colour scale represents characteristic Raman signal. The map and the spectra associated to it were processed using the software WITec Project version 2.08.

2.4. Fourier-transform infrared spectroscopy (FTIR)

Each sample was powdered and analysed by Fourier transform infrared spectroscopy (FTIR) in attenuated total reflection (ATR) mode, using a diamond cell. The equipment used was an infrared spectrometer Bomem MB-120 equipped with DTGS detector in the CCiT-UB. The resulting spectra are the sum of the 30 scans collected from 4000 to 350 cm^{-1} at a resolution of 4 cm^{-1}.

3. Results and discussion

3.1. Thermal behaviour of Ni-phyllosilicates

For the garnierite samples, the DTA-TG curves are shown in Fig. 3a–f and the endothermic and exothermic peaks and mass loss values are listed in Table 2. For the crystalline 1:1 and 2:1 Mg-phyllosilicate samples, the DTA-TG curves are presented in Fig. 4a–e, respectively, and the values are listed in Table 3.

Garnierite types I and II show similar DTA and TG curves, with two weak endothermic peaks at low temperatures (at 80 °C in type I, 109 °C in type II), and at 624–635 °C, and a strong exothermic peak at 816–817 °C (Fig. 3a-b, Table 2). In both garnierite types mass loss is produced in three steps: 3.4–3.74, 9.0–9.52 and 1.1–1.88 wt% (Fig. 3a–b,

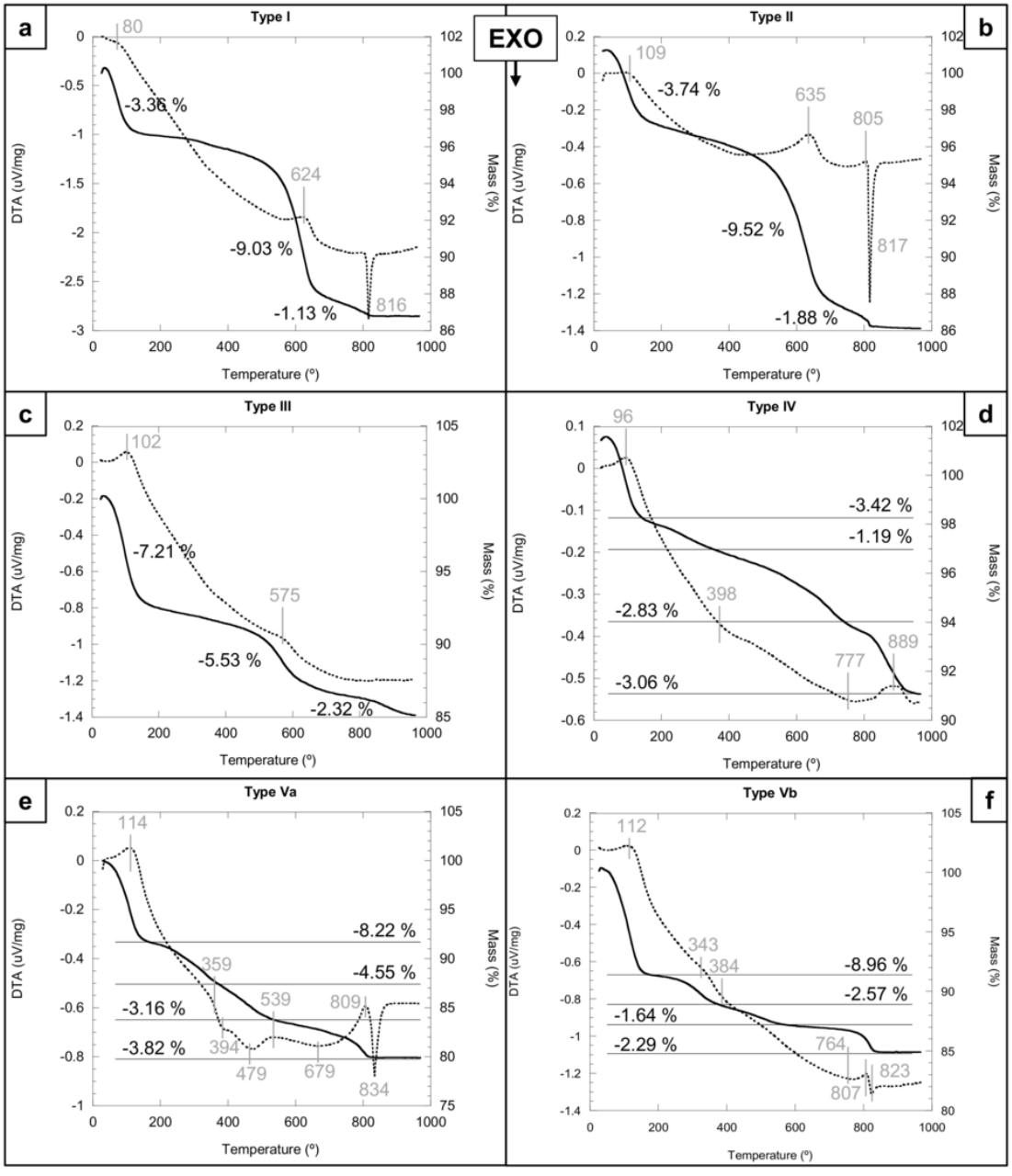

Fig. 3. DTA (dashed lines, data in grey) and TG (solid lines, data in black) curves of the garnierite samples selected for this study: a) type I (sample RD-1a), b) type II (LC-100A2), c) type III (GAR-2), d) type IV (LC-100A2), e) type Va (FALC-4), f) type Vb (FALC-3).

Table 2
Differential thermal analysis (DTA) results and thermogravimetry (TG) losses in weight percent (T = temperature; exo = exothermic; endo = endothermic) of the garnierite samples analysed: a) type I (RD-1a), b) type II (LC-100A2), c) type III (GAR-2), d) type IV (LC-100A2), e) type V – Ni-sepiolite (FALC-4) f) type V – falcondoite (FALC-3).

Type I		Type II		Type III		Type IV		Type Va		Type Vb	
T (°C)	DTA peak	T (°C)	DTA peak	T (°C)	DTA peak	T (°C)	DTA peak	T (°C)	DTA peak	T (°C)	DTA peak
80	endo	108.9	endo	102.2	endo	96.3	endo	114.4	endo	112.1	endo
624.4	endo	635	endo	575.1	endo	397.9	exo	359.4	endo	343	endo
816.3	exo	804.7	endo			776.6	exo	394.4	exo	383.9	exo
		816.9	exo			888.9	endo	479.4	exo	541.9	endo
								539.4	endo	763.7	exo
								679.4	exo	807.4	endo
								809.4	endo	823	exo
								834.4	exo		

Type I		Type II		Type III		Type IV		Type Va		Type Vb	
T range (°C)	TG loss (%)	T range (°C)	TG loss (%)	T range (°C)	TG loss (%)	T range (°C)	TG loss (%)	T range (°C)	TG loss (%)	T range (°C)	TG loss (%)
25–130	3.36	25–180	3.74	25–170	7.21	25–180	3.42	25–200	8.22	25–170	8.96
130–690	9.03	180–700	9.51	170–625	5.53	180–380	1.19	200–390	4.55	170–400	2.57
690–1000	1.13	700–1000	1.88	625–1000	2.32	380–745	2.83	390–525	3.16	400–645	1.64
						745–1000	3.06	525–1000	3.82	645–1000	2.29

Table 2). In general, the DTA and TG curves obtained are comparable to the curves for serpentine group minerals in the literature (Caillère and Hénin, 1957b; Viti, 2010; Fritsch et al., 2016), but the last mass loss can be assigned to the presence of a talc-like mineral (Figs. 3a–b, 4d; Table 3). However, the endothermic and exothermic peaks for antigorite, lizardite, polygonal serpentine and chrysotile of Viti (2010) are at slightly higher temperatures than those obtained in type I garnierite (likely due to different serpentine polytypes). The peaks in the range of 550 to 800 °C occur at relatively low temperatures (620 °C), more similar to the thermal effects of chrysotile than to those of antigorite, lizardite or polygonal serpentine (Viti, 2010). Fritsch et al. (2016) also found higher temperatures for chrysotile (650 °C) and antigorite (670 °C). The TG curve is similar to that presented in Sufriadin et al. (2012) for sample KR-1, composed mainly of lizardite and/or chrysotile and kerolite-pimelite.

Type III garnierite has two endothermic peaks at 102 and 575 °C (Fig. 3c, Table 2). Mass loss is performed in three steps: 7.21, 5.53 and 2.32 wt% (Fig. 3f, Table 2). The DTA curve is similar to that of talc (Caillère and Hénin, 1957a). The TG curve is comparable to those of serpentine group minerals, but with a larger initial mass loss (Fig. 4a–c, Table 3).

Type IV garnierite shows smooth endothermic peaks at 96 and 889 °C and exothermic peaks at 398 and 777 °C are observed. Mass loss is performed in four steps: 3.42, 1.19, 2.83 and 3.06 wt% (Fig. 3d, Table 2). The remarkable mass loss at low temperatures of this sample contrasts with that of talc, of only about 6 wt% above 800 °C (Fig. 4d, Table 3). Fritsch et al. (2016) also obtained a total mass loss of ~10 wt% in talc-dominated garnierites. In addition, the differential thermal analysis is different from that of talc, in which only a strong endothermic peak at about 1000 °C appears (Caillère and Hénin, 1957a; Fig. 4d, Table 3).

The rapid mass loss at low temperatures (near 100 °C), also related to the first endothermic peak, is related to the loss of hygroscopic (adsorbed) water (Brindley and Hang, 1973). The loss at higher temperatures, around 600 °C in serpentine-containing garnierites (types I to III) and around 900 °C in garnierites with remarkable amounts of a talc-like fraction (types III to IV), corresponds to the loss of structural water or dehydroxylation (Caillère and Hénin, 1957a, 1957b; Brindley and Hang, 1973). This was also related to the presence of mixtures of crystalline serpentines (mostly lizardite) and serpentine-like minerals by Fritsch et al. (2016). Indeed, these authors have noted that the endothermic peak related to the dehydroxylation of talc-like minerals is barely discernible, particularly at high serpentine contents (e.g., garnierite type I), as it interferes with the intense exothermic peak at about 825 °C generated by the breakdown of serpentine and the formation of anhydrous silicates.

The large initial mass loss of type IV garnierite near 200 °C (compared to that of talc in Caillère and Hénin, 1957a) suggest that the mineral contains extra water in the structure. This is coherent with the low oxide totals (sum of oxide wt% in EMP analyses) observed in type IV garnierite, suggesting that it consists of hydrated talc (kerolite-pimelite series) rather than of a standard talc (talc-willemseite series). In addition, as stated by Brindley and Hang (1973), the separation between dehydroxylation water (OH, structural water) loss and the monohydrate water (H_2O, the extra water in the kerolite-pimelite structure) loss is unclear. According to these authors, monohydrate water is lost from 110 to 700 °C. At first, the additional water, so-called "monohydrate water", was thought to occupy interlayer positions based on the 001 reflection at ~10 Å (like cations in micas) (Brindley and Hang, 1973). However, afterwards some data stated that the 001 reflection was at ~9.5–9.6 Å, so the last explanation is either invalid or incomplete. Much of the excess water is removable at temperatures up to 300 °C and probably occupies external positions (Brindley et al., 1979). The presence of molecular water in kerolite and pimelite was proven by IR spectrometry with the absorption in the 1900 cm^{-1} band (Brindley et al., 1979). The large surface area of these minerals and the small crystal size are coherent with a large amount of adsorbed water (Brindley, 1978). The slightly increased spacing with respect to that of talc (9.35 Å) may account for random layer stacking in kerolite-pimelite (Brindley, 1978). Hence, for this type of phase (the talc-like component), the terms kerolite and pimelite are more appropriate than talc and willemseite. Despite kerolite and pimelite were discredited by CNMMN-IMA (Nickel and Nichols, 2009, http://www.materialsdata.com), they are included in the recommendations for the nomenclature of phyllosilicates by the Association Internationale Pour l'Étude des Argiles (AIPEA; Guggenheim et al., 2006) and these names are still used nowadays (Tauler et al., 2009; Wells et al., 2009; Galí et al., 2012; Villanova-de-Benavent et al., 2014, 2016; Cathelineau et al., 2015). As a conclusion, given the DTA-TG presented in this work and previous EMP results (Villanova-de-Benavent et al., 2014), the garnierite type IV might actually be a mineral of the kerolite-pimelite solid solution series.

The TG curve of Ni-sepiolite and falcondoite is characterised by a mass loss in four steps (8.22, 4.55, 3.16, 3.82 wt% for Ni-sepiolite and

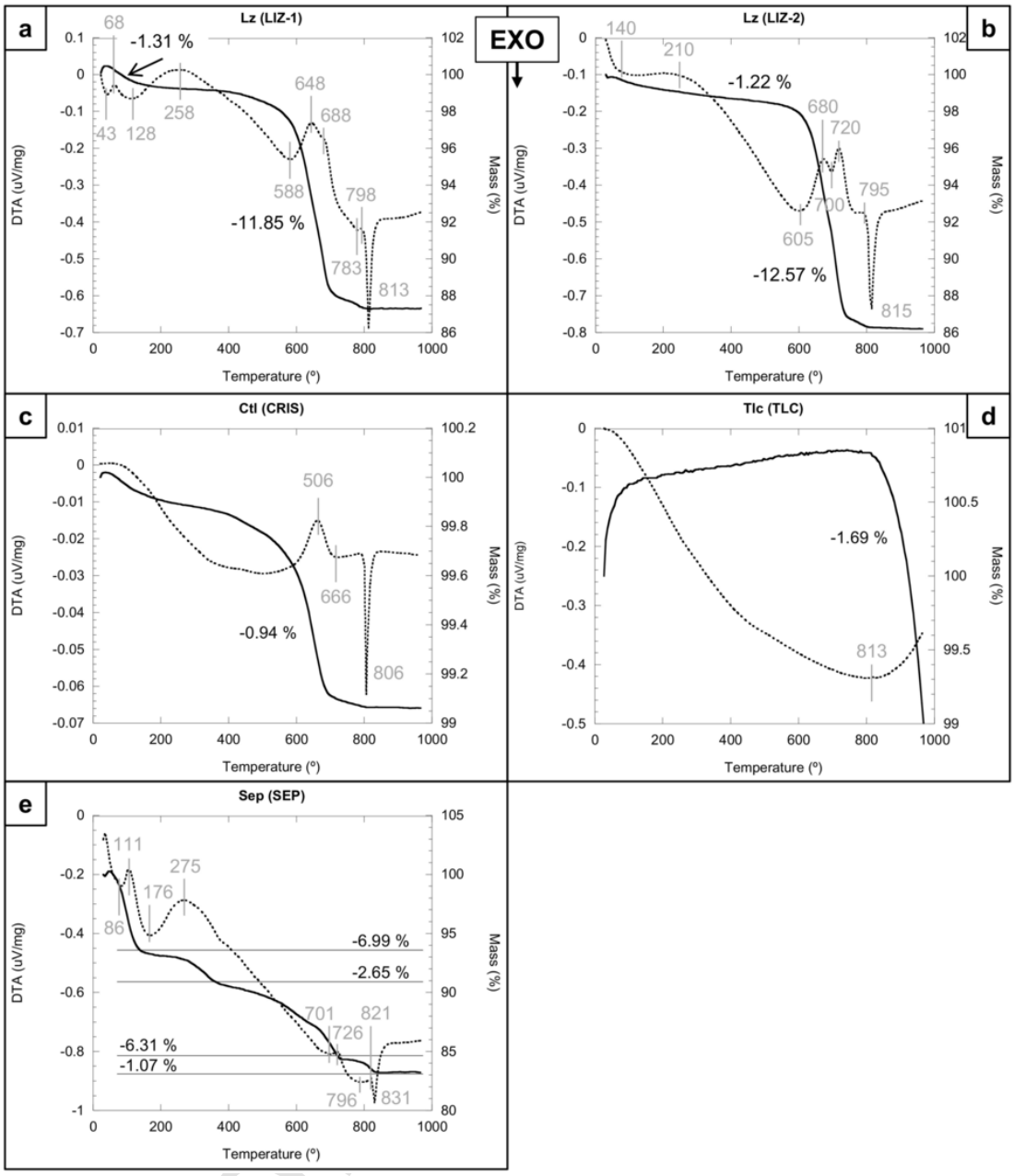

Fig. 4. DTA (dashed lines, data in grey) and TG (solid lines, data in black) curves of the 1:1 and 2:1 crystalline Mg-phyllosilicate samples selected for this study: a) lizardite (LIZ-1, Cornwall), b) lizardite (LIZ-2, Elba island), c) chrysotile (CRIS, Huelva), d) talc (TLC, León), e) sepiolite (SEP, Setcases). Legend: Lz = lizardite, Ctl = chrysotile, Tlc = talc, Sep = sepiolite.

8.96, 2.57, 1.64, 2.29 wt% for falcondoite) (Fig. 3e–f, Table 2), which do not show the typical ratios 6:4:3:1 (Caillère and Hénin, 1957c; Tauler et al., 2009). The DTA curves show that each step of water loss corresponds to an endothermic peak (at 112–114, 343–359, 539 and 807–809 °C), with a strong exothermic peak at 823–834 °C.

These curves are comparable to the sepiolite reference analysed in this study (Fig. 4e, Table 3) and to the published TG curves of Ni-sepiolites and falcondoites (Caillère and Hénin, 1957c; Springer, 1976; Tauler et al., 2009; Fritsch et al., 2016). According to Caillère and Hénin (1957) and references therein, mass loss at low temperatures represents the loss of zeolitic and/or hygroscopic water. Frost and Ding (2003), suggest that the peak at 200 °C corresponds to the loss of adsorbed water and possibly to the beginning of the loss of structural water. The peaks at the region 300–600 °C indicate the loss of coordinated water (Nagata et al., 1974). The endothermic peak at 807–809 °C corresponds to the dehydroxylation of the structure, and the exothermic peak at 823–834 °C to the formation of pyroxene (Jones and Galán, 1988).

3.2. Raman spectra of Ni-phyllosilicates

In this work the description of Raman data is divided into a) the low frequency region (100–1000 cm^{-1}), which depicts the bonds between atoms in inorganic materials; and b) the high frequency region (> 3300 cm^{-1}), involving OH stretching vibrations. The Raman spectra of garnierite samples is shown in Figs. 5a–e and 6a–f (obtained with the 1064 and 532 nm lasers, respectively) and those of the crystalline 1:1 and 2:1 Mg-phyllosilicate reference samples are included in Fig. 6g–k (with the 532 nm laser). All Raman bands and the corresponding assignments are shown in Table 4.

Table 3
Differential thermal analysis (DTA) results and thermogravimetry (TG) losses in weight percent (T = temperature; exo = exothermic; endo = endothermic) of the reference samples analysed: a) lizardite (LIZ-1 and LIZ-2), b) chrysotile (CRIS), c) talc (TLC), d) sepiolite (SEP).

lizardite (LIZ-1)		lizardite (LIZ-2)		chrysotile (CRIS)		talc (TLC)		sepiolite (SEP)	
T (°C)	DTA peak	T (°C)	DTA peak	T (°C)	DTA peak	T (°C)	DTA peak	T (°C)	DTA peak
42.7	exo	140.1	exo	506.4	exo	812.6	exo	85.5	exo
67.7	endo	210.1	endo	666.4	endo			110.5	endo
127.7	exo	605.1	exo	806.4	exo			175.5	exo
257.7	endo	680.1	endo					275.5	endo
587.7	exo	700.1	exo					700.5	exo
647.7	endo	720.1	endo					725.5	endo
687.7	endo	795.1	endo					795.5	exo
782.7	exo	815.1	exo					820.5	endo
797.7	endo							830.5	exo
812.7	exo								

lizardite (LIZ-1)		lizardite (LIZ-2)		chrysotile (CRIS)		talc (TLC)		sepiolite (SEP)	
T range (°C)	TG loss (%)	T range (°C)	TG loss (%)	T range (°C)	TG loss (%)	T range (°C)	TG loss (%)	T range (°C)	TG loss (%)
25–300	1.31	25–300	1.22	25–200	0.94	800–1000	1.69	25–200	6.99
300–800	11.85	300–800	12.57					200–400	2.65
								400–750	6.31
								750–1000	1.07

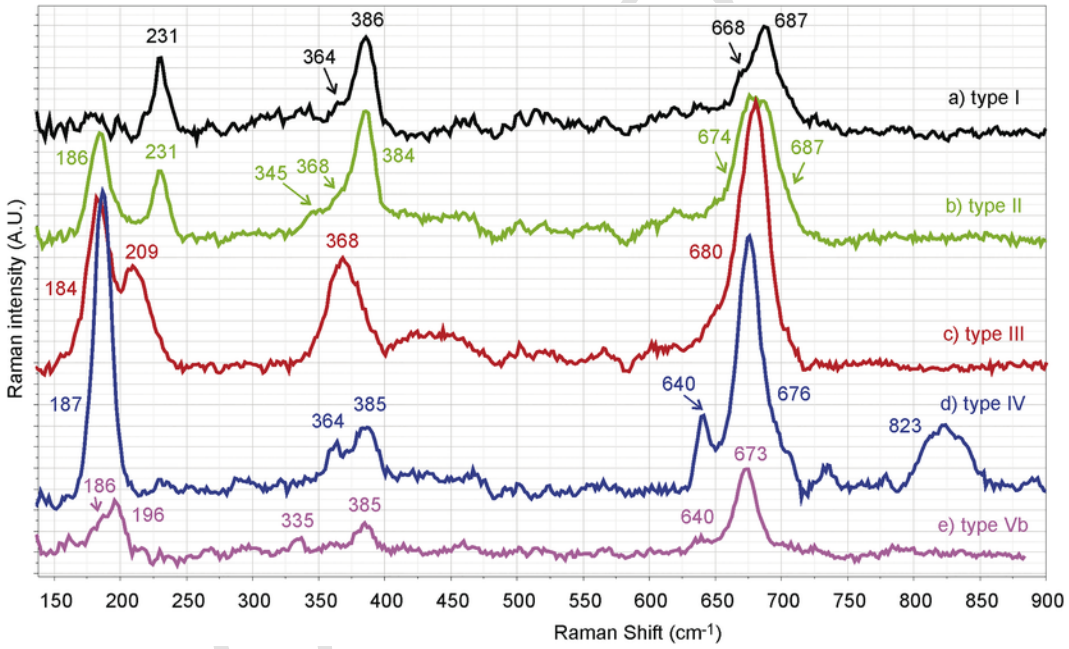

Fig. 5. Micro-Raman spectra of the five garnierite types described, obtained with the 1064 nm laser: a) type I (sample 09GAR-2), b) type II (sample LC-100), c) type III (sample GAR-2), d) type IV (sample GAR-6), e) type Vb (sample FALC-3).

3.2.1. Low frequency region (100–1000 cm^{-1})

The serpentine-dominated garnierites (types I and II) are characterised by the presence of strong Raman bands at 229–236, 382–389 and 687–692 cm^{-1}, and weaker bands and/or shoulders at 364–368 cm^{-1} (Figs. 5a–b, 6a–b, Table 4). The peaks at ~230 and ~385 cm^{-1} can be assigned to either serpentine group minerals or talc (Table 4), although they are less intense (or even absent) when the garnierite contain high amounts of kerolite-pimelite (or when the sample consists uniquely of kerolite-pimelite) (Figs. 5a–d, 6a–d, Table 4). These two bands are observed in the lizardite and chrysotile reference samples (Fig. 6g–i), and are absent in talc and sepiolite reference samples (Fig. 6j and k, respectively). In the literature, the band at ~230 is attributed to either metal-oxygen (M—O, Kloprogge et al., 1999) or O—H—O vibrations (Rinaudo et al., 2003; Groppo et al., 2006); the peak at ~344 to M—O (Kloprogge et al., 1999) or SiO_4 bending (Rinaudo et al., 2003; Groppo et al., 2006), the band at ~385 to M—O (Kloprogge et al., 1999) or symmetric SiO_4 vibrations (Rinaudo et al., 2003; Groppo et al., 2006), and the one at ~690 to Si—O vibrations (Kloprogge et al., 1999; Rinaudo et al., 2003; Groppo et al., 2006), all in serpentine minerals (Table 4). Apart from this, the band at ~345 cm^{-1} in type II could be related to that at 356 cm^{-1} of chrysotile (this study), and it was related to both lizardite and chrysotile by Kloprogge et al. (1999) and Groppo et al. (2006), and to chrysotile by Rinaudo et al. (2003). Finally, the broad 823 band has been attributed to Ni—OH deformation (Frost et al., 2008; Table 4).

Type III garnierite has a strong band at 679–680 cm^{-1}, but the other intense bands shown by type I and II are absent. In contrast, it shows intense bands at around 182–184 cm^{-1}; and a slightly less intense band at 367–368 cm^{-1} in both 1064 and 532 nm laser spectra. Another peak

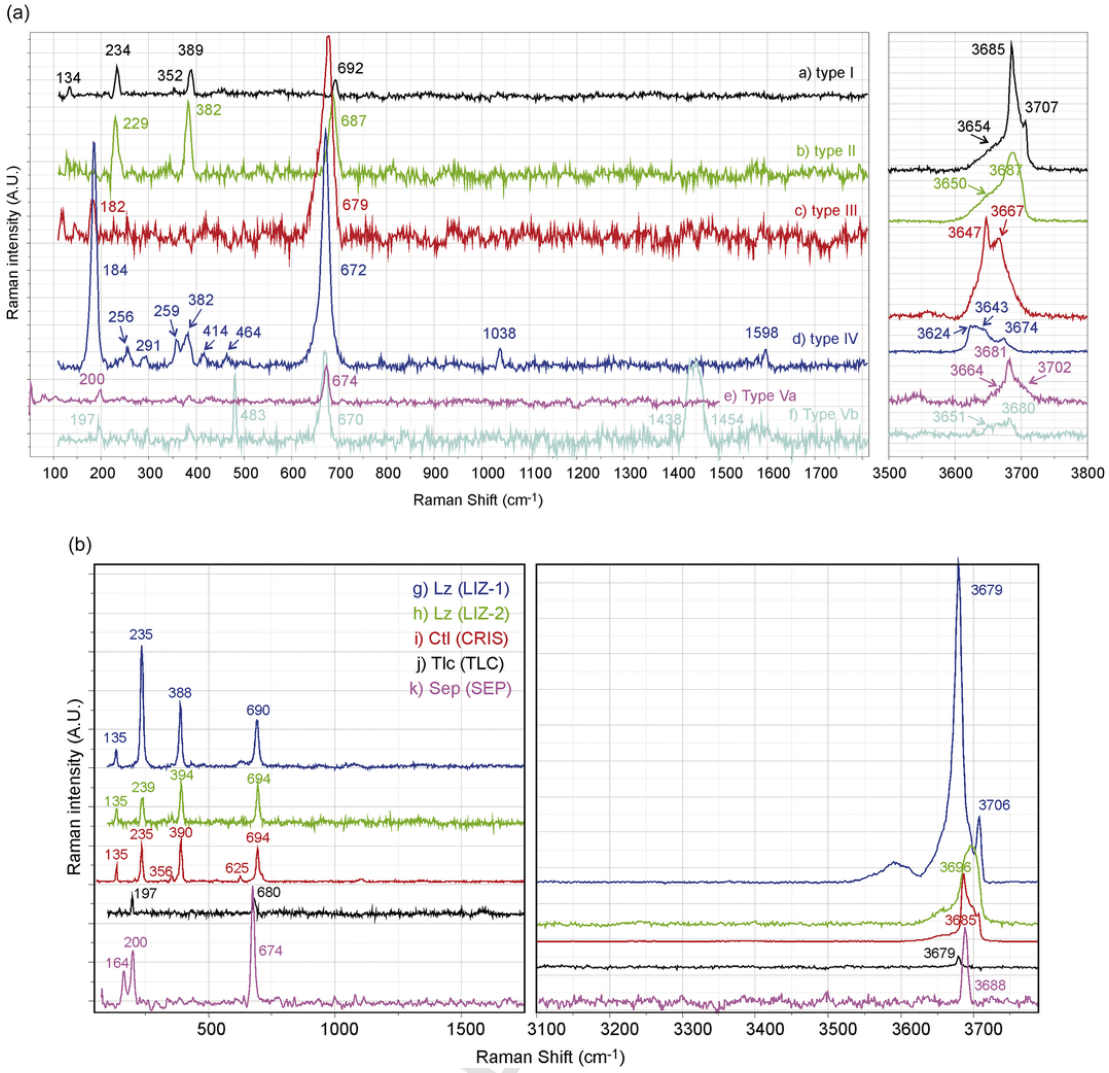

Fig. 6. Micro-Raman spectra of the five garnierite types described, obtained with the 532 nm laser: a) type I (sample 09GAR-2), b) type II (sample LC-100), c) type III (sample GAR-2), d) type IV (sample LC-100), e) type Va (sample FALC-4), f) type Vb (sample FALC-3). Micro-Raman spectra of the crystalline 1:1 and 2:1 Mg-phyllosilicates analysed for comparison, obtained with the 532 nm laser: g) lizardite (Lz, sample LIZ-1, Cornwall), h) lizardite (Lz, sample LIZ-2, Elba island), i) chrysotile (Ctl, sample CRIS, Huelva), j) talc (Tlc, sample TLC, León), k) sepiolite (Sep, sample SEP, Setcases).

at 209 cm^{-1} was produced by the 1064 nm laser, which is exclusively related to serpentine (Groppo et al., 2006; Fig. 6c, Table 4). The shifted position of the serpentine M—O Raman band to lower wavelengths from ~230 cm^{-1} down to 209 cm^{-1} when comparing samples type I/II to type III may be correlated with the disappearance of the polygonal serpentines present in types I and II and the development of bent lamellae of serpentine present in type III in agreement with the results obtained by means of high resolution TEM on equivalent samples (Villanova-de-Benavent et al., 2016).

In contrast, type IV garnierite with dominant kerolite-pimelite presents high intensity bands at 184–187 and 672–676 cm^{-1}, and less intense bands at 364, 382–385, 640 and 823 cm^{-1} (Figs. 5d, 6d). The occurrence of talc-like particles in the garnierite samples is stated by the bands at 184–187 and 364 cm^{-1} (Figs. 5b-d, 6b–d, Table 4). Both are found in the talc reference sample (Fig. 6j). The peak at 364 cm^{-1} is assigned to the M—O vibrations in talc (Blaha and Rosasco, 1978) and that at 672–676 cm^{-1} corresponds to O—Si—O bridging/Si—O—Si symmetric stretching in talc (Blaha and Rosasco, 1978; Rosasco and Blaha, 1980; Table 4). These characteristic talc bands were also observed in type I, II and III garnierites, like the weak bands at 364–368, confirming the presence of variable amounts of talc-like particles in the samples. Therefore, even though the talc-like was not identified by powder XRD in type I garnierite, the particles were observed by TEM and can be detected by Raman spectroscopy (shoulder at 364 cm^{-1} in Fig. 5a). In type II, the new appearing band at 179–186 cm^{-1} is more intense than the band at 229–231 cm^{-1}, and the former decreases slightly in intensity when compared to the same band in type I. This can be indicative of a higher amount of talc than serpentine in the sample for the analysed spot, and a decrease of serpentine in type II when compared to type I (Figs. 5b, 6b).

The two Si—O bands in the range between 668 and 692 cm^{-1} deserve special attention, and are present in all five garnierite types. Both 668–674 and 687–692 cm^{-1} peaks are observed in type I and II garnierites, the latter being more intense in type I. A band in-between these two, at 680 cm^{-1}, is shown in type III garnierites (Figs. 5c, 6c), and only the peak at 672–676 cm^{-1} is observed in type IV garnierites (Figs. 5d, 6d).

Therefore, the higher Raman band shifts in this range may be characteristic of serpentine minerals, whereas bands at lower Raman shifts may be related to talc-like phases; which is coherent with This Blaha and Rosasco (1978), Rosasco and Blaha (1980), Kloprogge et al.

Table 4
List of the Raman bands detected using the 1064 and 532 nm lasers in the garnierite samples, compared to the Raman bands obtained from the Mg-phyllosilicates from other localities and Mg-Ni-phyllosilicates from the literature (legend: s = strong, m = medium, w = weak, sh = shoulder, d = doubtful; Srp = serpentine, Lz = lizardite, Nép = népouite, Ctl = chrysotile, Pec = pecoraite, Atg = antigorite, PS = polygonal serpentine, Tlc = talc, Ker = kerolite, Sep = sepiolite). The laser wavelength used in the references is indicated in brackets.

This study - 1064 nm					This study - 532 nm						This study - 532 nm					Ctl (a, 633 nm)	Srp (b, 514.5 nm)	Srp (c, 1064 nm)
Type I (09GAR-2)	Type II (LC-100)	Type III (GAR-2)	Type IV (GAR-6)	Type Vb (FALC-3)	Type I (09GAR-2)	Type II (LC-100)	Type III (GAR-2)	Type IV (LC-100)	Type Va (FALC-4)	Type Vb (FALC-3)	Lz (LIZ-1)	Lz (LIZ-2)	Ctl (CRIS)	Tlc (TLC)	Sep (SEP)			
					134.0 **m**						135.1 **w**	135.1 **w**	135.1 **m**			–	–	–
															164.0 **m**	–	–	–
	186.1 **s**	183.6 **s**	186.7 **s**	186.4 **sh**			182.4 **w**	184.2 **s**									–	–
				195.5 **s**					199.9 **w**	196.5 **w**				196.6 **s**	200.0 **m**	M-O	–	A1g mode of Mg(O,OH)6 in Ctl (Kloprogge et al., 1999)
		209.3 **m**														–	–	–
230.6 **s**	230.5 **s**				235.7 **m**	229.1 **s**					234.7 **s**	239 **m**	235.3 **s**			M-O	lattice and interval vibrational modes (weak in Lz, strong in Ctl, Atg, PS)	vibrations of O-H-O groups in Srp (also Kloprogge et al., 1999)
								255.6 **w**								–	–	–
							271.3 **w**									–	–	–
								291.4 **w**								–	–	–
				333.8 **w**												–	–	–
	344.6 **sh**							359.4 **m**					355.9 **w**			M-O	–	bending of SiO_4 in Ctl, Lz (also Kloprogge et al., 1999)
364.4 **sh**	367.7 **sh**	368.4 **m**	363.9 **w**				366.4 **w**									–	–	–
385.8 **s**	384.2 **s**		385.1 **w**	384.9 **w**	388.8 **m**	382.2 **s**		382.0 **m**			388.3 **m**	394.2 **s**	389.8 **s**			M-O	lattice and interval vibrational modes in Srp	symmetric v5(e) SiO4 in Srp (also Kloprogge et al., 1999)

	414.3**w**		–	lattice and interval vibrational modes in Srp	–	–

Table 4 (*Continued*)

This study - 1064 nm					This study - 532 nm						This study - 532 nm					Ctl (a, 633 nm)	Srp (b, 514.5 nm)	Srp (c, 1064 nm)
Type I (09GAR-2)	Type II (LC-100)	Type III (GAR-2)	Type IV (GAR-6)	Type Vb (FALC-3)	Type I (09GAR-2)	Type II (LC-100)	Type III (GAR-2)	Type IV (LC-100)	Type Va (FALC-4)	Type Vb (FALC-3)	Lz (LIZ-1)	Lz (LIZ-2)	Ctl (CRIS)	Tlc (TLC)	Sep (SEP)			
								463.9**w**		482.5**s**						–	lattice and interval vibrational modes in Srp	–
													625.2**w**			–	lattice and interval vibrational modes in Srp	antisymmetric OH-Mg-OH translation modes in Ctl (Kloprogge et al., 1999)
			639.6**m**	639.5**w**												–	–	–
668.2**sh**	674.3**s**	680.4**s**	675.9**s**	673.4**s**			678.6**s**	671.7**s**	674.1**s**	669.6**s**				679.6**s**	674.0**s**	–	–	–
686.5**s**	686.5**s**				692.2**m**	686.5**s**					689.8**m**	694.2**m**	694.2**s**			Si-O bridging or stretching, also 692 Lewis (1996) and 622 Bard (1997)	–	vs Si-Ob-Si in Srp (also Kloprogge et al., 1999)
			822.9**m**													–	–	–
								1038.0**m**								–	–	–
																–	–	–
																–	–	–
										1438.2**s**						–	–	–
										1454.6**s**						–	–	–
								1597.6**w**								–	–	–
																–	–	–
								3624**s**								–	internal stretching vibration of OH groups (weak in Atg)	–
								3632**s**								–	–	–

Table 4 (*Continued*)

This study - 1064 nm					This study - 532 nm						This study - 532 nm					Ctl (a, 633 nm)	Srp (b, 514.5 nm)	Srp (c, 1064 nm)
Type I (09GAR-2)	Type II (LC-100)	Type III (GAR-2)	Type IV (GAR-6)	Type Vb (FALC-3)	Type I (09GAR-2)	Type II (LC-100)	Type III (GAR-2)	Type IV (LC-100)	Type Va (FALC-4)	Type Vb (FALC-3)	Lz (LIZ-1)	Lz (LIZ-2)	Ctl (CRIS)	Tlc (TLC)	Sep (SEP)			
					3654**sh**	3650**sh**	3647 **s**	3643 **s**		3651**w**						inner OH stretch	–	–
							3667 **s**	3674 **m**	3664**w**							OH stretch, also 3685 Bard (1997)	internal stretching vibration of OH groups (Atg)	–
					3685 **s**	3687 **s**			3681**w**	3680**w**	3679 **s**		3685 **s**	3679 **m**	3688 **s**	OH stretch or external OH stretch, also 3700 Bard (1997)	internal stretching vibration of OH groups (Lz, shoulder in Ctl and PS)	–
					3707 **m**				3702**w**		3706**w**	3696 **s**				–	internal stretching vibration of OH groups (Lz, Ctl, Atg, PS)	–

(a) Kloprogge et al. (1999), (b) Auzende et al. (2004), (c) Rinaudo et al. (2003), (d) Groppo et al. (2006), (e) Frost et al. (2008), (f) Fritsch et al. (2016), (g) Blaha and Rosasco (1978), (h) Rosasco and Blaha (1980), (i) Cathelineau et al. (2015), (j) McKeown et al. (2002), (k) RRUFF

(1999), Rinaudo et al. (2003), Groppo et al. (2006), and the RRUFF database.

Finally, sepiolite-falcondoite is easily identifiable by the band at 196–200 cm^{-1}, which is lacking in the other garnierite types. The bands at 385, 640 and 670–674 cm^{-1} are also observed in the other garnierites (Figs. 5e, 6e–f), and the Si—O band (670–674 cm^{-1}) is present at even lower Raman shifts than in type IV garnierite (672–676 cm^{-1}) (Fig. 5d, Table 4). In addition, the Ni-bearing sepiolite and falcondoite patterns are similar to that of the reference sepiolite (Fig. 6k, Table 4). Bands at ~200, ~650 and ~1100 cm^{-1} have also been observed in sepiolite by McKeown et al. (2002), and a broad peak at ~670 cm^{-1} is also seen in the RRUFF database (sepiolite, ID R070311). However, a band at ~250 cm^{-1} is present in both references, but not in the samples analysed in this study (Fig. 6k).

In the low frequency region of Raman spectra, the effect of the Ni content of Ni-bearing phyllosilicates is difficult to unravel. Wang et al. (2002) explained the influence of the cations in the octahedral site and the position of the bands in the range < 600 cm^{-1} in phyllosilicates. Most Fe-bearing phyllosilicates show a wide, strong band at ~550 cm^{-1}, most Al-bearing have a wide, strong peak at ~420, and most Mg-bearing show a strong peak at ~350 cm^{-1}. Therefore, the Ni content in phyllosilicates may have a characteristic Raman effect on the garnierite patterns. However, by comparing the garnierite spectra with the crystalline, Ni-free serpentine, talc and sepiolite patterns, no significant differences were found which could be attributed to the presence of Ni in the minerals.

3.2.2. The high frequency region (> 3300 cm^{-1})

Serpentine-dominated garnierites (types I and II) display a strong band at 3685–3687 cm^{-1} and a shoulder at 3650–3650 cm^{-1}. The latter is present as a strong band in type III (at 3647 cm^{-1}) and type IV (at 3643 cm^{-1}) garnierites, in addition to another band at 3667 cm^{-1} in type III and at 3674 cm^{-1} in type IV. Both Ni-sepiolite and falcondoite have a weak band at 3680–3681 cm^{-1}, although Ni-sepiolite has also weak bands at 3664 and 3702 cm^{-1}, and falcondoite at 3651 cm^{-1} (Fig. 6, Table 4).

All these bands are often assigned in the literature to OH stretching or OH vibration of phyllosilicates (Kloprogge et al., 1999; Wang et al., 2002; Auzende et al., 2004; Frost et al., 2008; Fritsch et al., 2016; Blaha and Rosasco, 1978; Rosasco and Blaha, 1980; Cathelineau et al., 2015; Table 4). The number of OH peaks, their positions and their relative intensities are controlled by the number and types of OH sites and the types of cation occupancies around OH groups (Wang et al., 2002). In particular, the band at ~3640 cm^{-1} was identified in chrysotile (Kloprogge et al., 1999; Frost et al., 2008), pecoraite (Frost et al., 2008). The band at ~3670 cm^{-1} was found in the lizardite from Cornwall (Fig. 6g), in chrysotile (Kloprogge et al., 1999) and talc (Blaha and Rosasco, 1978; Rosasco and Blaha, 1980; Fig. 6j). The band at ~3680 cm^{-1} was observed in chrysotile (Kloprogge et al., 1999; Fig. 6i). Finally, a band at 3700 cm^{-1} was identified in lizardite (Fig. 6h), chrysotile and pecoraite (Frost et al., 2008) and kerolite (Cathelineau et al., 2015) (Fig. 6g, Table 4).

In addition, some authors use the high Raman frequency region to distinguish among species of the serpentine group (Petriglieri et al., 2014, 2015). Petriglieri et al. (2015) found that chrysotile and polygonal serpentine have similar Raman spectra in this region, characterised by a very strong peak (at 3698 in chrysotile and at 3697 in polygonal serpentine) and a shoulder (at 3691 and 3689, respectively), and preceded by a very weak peak (at 3651 cm^{-1} and 3646 cm^{-1}). In contrast, lizardite had a weak band at 3660 preceding a strong band at 3683 with a shoulder at 3703 cm^{-1} (Petriglieri et al., 2015). The bands in type I and II garnierites are comparable to those of lizardite reported by Petriglieri et al. (2015) and that of the reference sample (Table 4); but can also be assigned to chrysotile (Kloprogge et al., 1999; Auzende et al., 2004; Fritsch et al., 2016) and polygonal serpentine (Auzende et al., 2004).. It is worth noting that the spectrum of lizardite from Cornwall (Fig. 6g) resembles that of lizardite in Petriglieri et al. (2015), whereas the spectrum of lizardite from Elba Island (Fig. 6h) is similar to that of polygonal serpentine in the same article (Table 4); and the latter may contain chrysotile impurities (Lacinska et al., 2016).

Furthermore, Cathelineau et al. (2014, 2015) established that the position and intensity of the Raman bands in the high region was sensitive to the Ni content in the kerolite-pimelite series: the lower Ni contents are related to intense bands at higher positions (3670, 3685 and 3700 cm^{-1}, being the last the only band present when Ni is absent), and the higher Ni contents are associated to lower positions (3650, 3660 and a shoulder at 3625 cm^{-1}); being the intermediate Ni contents related to a complex band cluster with three major peaks at 3649, 3670 and 3700 cm^{-1}. On this basis, the bands observed in the Raman spectrum of type IV garnierite indicate that the point analysis may have been performed on an area with a remarkably high Ni content (Fig. 6d). In contrast, the bands in type III could be explained by the presence of a kerolite-pimelite with slightly less Ni (Fig. 6c). Finally, the sepiolite-falcondoite bands at ~3690 cm^{-1} were detected in this study (Fig. 6e, f, k, Table 4) but not in the literature for sepiolite.

3.2.3. Micro-raman map

The micro-Raman map was performed in an area containing type II and IV garnierites, a saprolite fragment (consisting of fine grained, low Ni serpentine with minor goethite and quartz) and quartz crystals filling a void (Fig. 7a–e).

Two Raman spectra associated to serpentine were distinguished, one corresponding to the saprolite fragments (in red) and the other to the type II garnierite (in navy blue) (Fig. 7d–e). Type IV garnierite (kerolite-pimelite) was easily identified as well (in green) (Fig. 7d–e), with its characteristic zoning visible in the integrated intensity image (Fig. 7c).

3.3. FTIR results

In the 500–800 cm^{-1} region (Fig. 8a, Table 5) the spectrum of type I and type II garnierites show two bands at 569 cm^{-1} and 606 cm^{-1} which are thought to be related to the Mg—OH libration and Mg—OH bending of chrysotile (Kloprogge et al., 1999; 2000) and/or lizardite (Baron and Petit, 2016). The absence of the band corresponding to the Ni—O libration at 674 cm^{-1} rules out the presence of népouite (Baron and Petit, 2016). In type III the band at 606 cm^{-1} still persists, but only as a shoulder, suggesting the progressive disappearance of the serpentine. New bands at 668 cm^{-1} and 710 cm^{-1} do appear corresponding to the Mg—OH and Ni—OH libration of talc and willemseite, respectively (Ishida, 1990). Type IV and V garnierite do still have the Mg—OH and Ni—OH libration band modes of talc and willemseite but the type V garnierite additionally shows bands at 780 cm^{-1} and 640 cm^{-1} close to the Mg—OH libration modes of sepiolite (Yeniyol, 2014).

In the lattice bands region (Fig. 8b, Table 6) the type I, II and III garnierites display two bands at 968 and 1030 cm^{-1} which are thought to be related to the Si—O stretching of chrysotile (Kloprogge et al., 1999, 2000) and probably lizardite (Baron and Petit, 2016). Type IV garnierite presents a large band in the region at 1000 cm^{-1} is thought to be related to the Si—O stretching in kerolite-pimelite (Brindley et al., 1979). Ni-sepiolite and falcondoite samples display two bands at 974 cm^{-1} and 1210 cm^{-1} that do sit close on the Si—O and Si—O—Si stretching bands of sepiolite (Yeniyol, 2014).

In the OH-stretching zone (Fig. 8c–d, Table 7) the type I and II garnierites present absorption bands at 1635 cm^{-1} corresponding to H_2O O—H—O bend (Frost et al., 2008), Mg—OH stretching (Kloprogge et al., 1999), absorbed H_2O bend (Kloprogge et al., 2000) in népouite, chrysotile and pecoratite. The band at 3645 cm^{-1} corresponds to OH

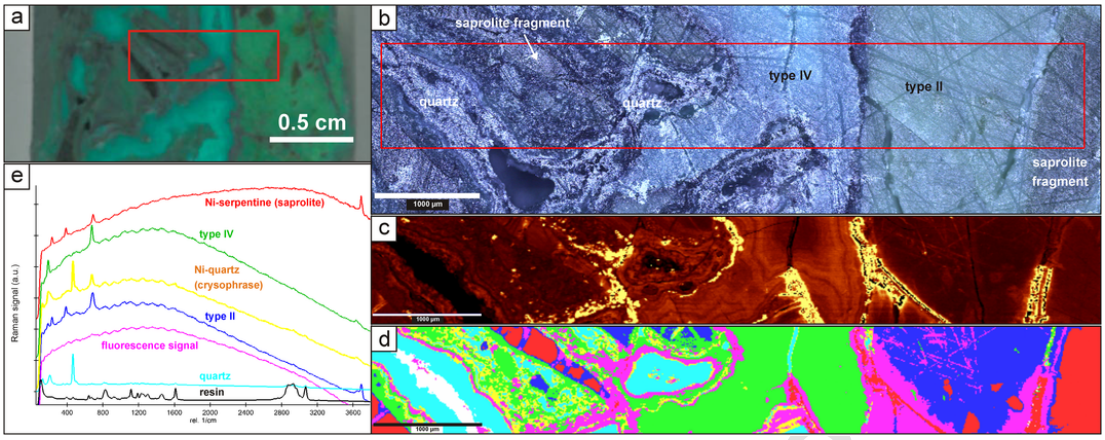

Fig. 7. Micro-Raman map on a selected area containing various garnierite types and other associated phases: a) image of the area on sample LC-100; b) reflected light photomicrograph showing the textural relationships between garnierite types II and IV, saprolite fragment and quartz crystals; c) false colour integrated intensity micro-Raman image in the range 150–750 cm^{-1} (brighter areas indicate higher Raman signal and/or higher fluorescence in this range); d) micro-Raman map; e) corresponding colour-coded spectra of each characteristic zone in d). Red rectangles indicate the scanned area. (For interpretation of the references to colour in this figure legend, the reader is referred to the web version of this article.)

stretching in lizardite, népouite, chrysotile, pecoratite and kerolite-pimelite (Baron and Petit, 2016; Capitani and Ventruti, 2018; Frost et al., 2008; Kloprogge et al., 2000; Brindley et al., 1979). The band at 3685 cm^{-1} is probably also corresponding to OH stretching in lizardite and/or chrysotile (Baron and Petit, 2016; Kloprogge et al., 1999, 2000). Type III garnierite has the same bands at 1635 cm^{-1} and 3645 cm^{-1} but missing the band at 3685 cm^{-1} corresponding to chrysotile (Kloprogge et al., 1999). Type IV garnierite presents bands at 1635 cm^{-1}, which may correspond to the adsorbed water in garnierite (Kloprogge et al., 2000 and references therein) and 3625 cm^{-1} corresponding to the OH stretching in kerolite-pimelite (Brindley et al., 1979). Ni-sepiolite and falcondoite samples display the bands at 1620 cm^{-1} corresponding to zeolitic water, at 3570 cm^{-1} and at 3625 cm^{-1} corresponding to the OH stretching in sepiolite (Yeniyol, 2014). Furthermore, variations were observed in the position of the FTIR bands that can be atributted to different configurations of water/OH in the structures of the studied garnierites. First, bands assigned to zeolitic water are characteristic of sepiolite-falcondoite, at 1620 (this study) and 1660 cm^{-1} (Yeniyol, 2014). Second, the bands in the range of 3400–3700 cm^{-1} in kerolite-pimelite are assigned to OH stretching (Brindley et al., 1979). These bands are observed in the serpentine-bearing garnierite types I to III (at 3645 cm^{-1}) and type IV, which consists of mostly kerolite-pimelite (at 3625 cm^{-1}, Table 7). Unfortunately, the adsorbed water bands at about 3400 cm^{-1} (Brindley et al., 1979) were not observed in this study. Finally, the OH stretching bands of serpentine-group minerals are present at around 3650 and 3700 cm^{-1} (Baron and Petit, 2016; Kloprogge et al., 1999; 2000), and they were observed in the serpentine-bearing garnierite types I to III (Table 7).

3.4. Implications of the study of natural garnierites in ore exploration and processing, and phyllosilicate synthesis

Firstly, pyrometallurgical processes used to obtain ferronickel from laterite ores are highly energy consuming, because the input material has to be dehydrated (including free moisture and structural water) and later calcined, using hydrocarbon fuels and/or electric power (Dalvi et al., 2004). Garnierites are only a part of the slag processed by pyrometallurgy to produce ferronickel, which is composed of about 1.5–2.5 wt% Ni, 10.5 Fe/Ni and 1.6 SiO_2/MgO, 25–35 wt% free moisture and 10–12% structural water (Warner et al., 2006; Swinbourne, 2014). In the furnace, the temperatures required to produce low carbon ferronickel (like the one obtained in Falcondo, Dalvi et al., 2004) are higher (1450–1460 °C) than those to produce high carbon ferronickel (1250–1350 °C) (Swinborne, 2014). However, the minimum temperature in the furnace is determined by the composition of the slag (in low carbon ferronickel, characterised by high Fe/Ni ratio and high MgO content). The SiO_2/MgO ratio has to be constrained to values below 2 and above 2.5, (avoiding the interval between 2.3 and 2.5, as it is corrosive to the furnace lining, Dalvi et al., 2004). Hence, a precise identification of the mineralogy of the slag (in terms of SiO_2/MgO and H_2O) could be ultimately beneficial to lower the energy consumption and to avoid undesirable SiO_2/MgO ratios and Fe contents. However, a chemical identification is insufficient in most cases, and should be coupled with a mineralogical identification. For this reason, portable X-ray fluorescence and Raman spectroscopy devides have been recently incorporated by mining companies during ore exploration, as they represent an excellent, rapid, easy-to-use, non-destructive methods for both chemical and mineralogical characterisation of samples in the field.

Nevertheless, the position of the bands in the interval 670–690 cm^{-1} gives information of the minerals that constitute the garnierite mixture. In serpentine-dominated mixtures, the band is near 690 cm^{-1}, whereas in kerolite-pimelite-dominated mixtures, the band is at about 670 cm^{-1}. As reported by Villanova-de-Benavent et al. (2016), the garnierites from the Falcondo mining district with higher talc fractions also contained the higher Ni concentrations. Therefore, the position of the aforementioned band at higher Raman shifts indicates the presence of abundant kerolite-pimelite and, in turn, in the case of Falcondo, suggests that the garnierite might be Ni-rich. This is significant, as a) it allows identifying indirectly the Falcondo garnierites with higher Ni contents; and b) it allows detecting possibly unwanted talc-like or kerolite-pimelite particles generated when synthesising Ni-Mg-phyllosilicates (in particular tubular structures like Ni-chrysotile), that might concentrate Ni (instead of Ni being deposited onto or incorporated in chrysotile). This also proves the importance of having a detailed, previous characterisation of the materials of each study area, to be used as internal standards to be compared with the analyses obtained in the field.

Secondly, it must be taken into account that natural garnierites are mixtures of phyllosilicates (mainly serpentine- and talc-like) and that at least in Falcondo, Ni is more concentrated in the talc-like phase of the mixture. A garnierite matching this description was studied as possible natural catalyst by Jacobs et al. (1980). To examine the catalytic activity, the mineral was reduced in hydrogen. During hydrogen activation (> 673 K), the serpentine and talc-like components of the mixture decomposed (although the latter is more stable), and Ni reduction occurred, so that Ni^0 particles formed first in the talc-like phase (higher reducibility) and later in the serpentine fibres (lower reducibility)

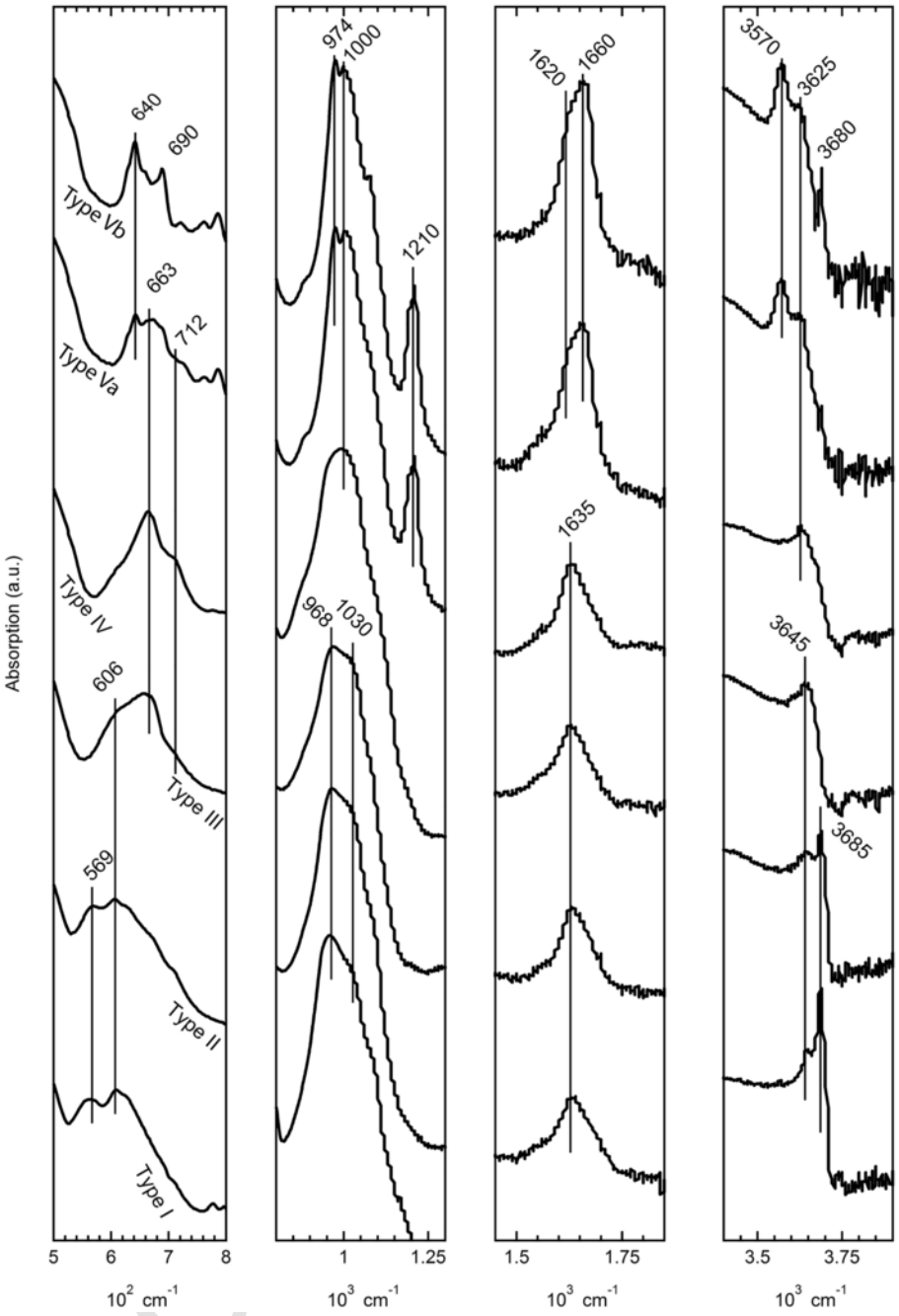

Fig. 8. FTIR absorption bands corresponding to the a) 500–800 cm^{-1} region, b) to the 800–1300 cm^{-1} region, c) and d) to the OH region (type I: 09GAR-2; type II: LC100B; type III: GAR-2; type IV: GAR-6; type Va – Ni-sepiolite: FALC-4; type Vb – falcondoite: FALC-3).

(Jacobs et al., 1980). Hence, the optimum reduction of Ni depends on the mineralogy of the garnierite mixture. Furthermore, energy models on the redistribution of cations in conical and cylindrical serpentine nanotubes (applied to Ni-doped synthetic minerals, but translatable to other cations such as Co and Fe) show that morphology (conical and cylindrical serpentines) and cation redistribution affect the stability of the minerals. This may inhibit recrystallisation when serpentines are long exposed to treatments in hydrothermal conditions (Krasilin and Gusarov, 2017). Therefore, even the morphology of the serpentine nanoparticle may affect the stability of the synthetic phyllosilicate and the mobility of Ni during catalytic reactions.

Consequently, a better knowledge, not only of the structure and chemical composition, but also of the thermal behaviour and Raman and FTIR spectroscopy response of natural garnierites could be used, for example: a) to check the composition of the slag undergoing pyrometallurgy processes (based on the mineralogy, in addition to the chemistry); b) to analyse the mineralogy (with a portable Raman spectrometer, coupled with a X-ray fluorescence device) on site in the field; and c) to constrain the mineralogy (different serpentine minerals, talc-like phases, sepiolite) and the distribution of Ni (in serpentine-/talc-like phase, structural, adsorbed) of either natural or synthetic phyllosilicate-supported catalysts. The techniques used in this study represent an inexpensive and easy method for Ni-Mg-phyllosilicate identification (structure, amount and distribution of water, proxy for structural Ni content), require no (Raman spectroscopy) or very simple (DTA-TG and FTIR) sample preparation, can be applied to small amounts of samples

Table 5
FTIR absorption bands corresponding to the 500–800 cm^{-1} region compared with Mg-Ni-phyllosilicates from the literature (* = weight percent calculated from the structural formula of the mineral analysed in the cited work, ** = weight percent presented in the cited work, *** = from the DTA-TG results in this study).

From literature										This study						
Lizardite	Népouite	Chrysotile	Pecoraite	Talc	Willemseite	Kerolite	Pimelite	Sepiolite	Garnierite	Type I	Type II	Type III	Type IV	Type Va	Type Vb	Assignment
-	500(c)	-	-	-	-	-	-	-	500(e)	-	-	-	-	-	-	(Mg,Ni)—O stretching (c), (Mg,Ni)—O (e)
-	536(c)	-	-	-	-	-	-	-	536(e)	-	-	-	-	-	-	Ni—O stretching (c), perpendicular Ni—O (e)
562(a)	-	550(d,e)	-	-	-	-	-	-	-	569	569	-	-	-	-	in-plane OH bending (a), Mg—O/Si—O bend (d)
607(a)	605(c)	607(d), 604(e)	607(c)	-	-	-	-	-	-	606	606	606	-	-	-	in-plane OH bending (a), Ni—OH libration (c), Mg—OH libration (d), (Mg,Ni)—OH libration (e)
-	-	-	-	-	-	-	-	649(h)	-	-	-	-	-	640	640	Mg—OH bending (h)
634(a)	-	654(d), 654-660(e)	628, 660(c), 647, 668(e)	-	-	-	-	-	672 (e)	-	-	-	-	-	-	in-plane OH bending (a), Ni—OH libration (c), Mg—OH libration (d), Si—O bridge (e)
-	674(a), 673 (b), 672 (c)	-	-	668(f)	-	670-700(g)	670-700(g)	-	-	-	-	663	663	663	-	Ni—OH libration (a,b,c), OH libration (f,g)
-	-	-	-	-	-	-	-	692(h)	-	-	-	-	-	-	690	Mg—OH bending (h)
-	-	-	707(e)	-	710(f)	-	-	-	-	-	-	712	712	712	-	Ni—OH translation (e), OH libration (f)
-	-	-	-	-	-	-	-	783(h)	-	-	-	-	-	780	780	Mg—OH bending (h)
-	-	-	820, 839(c), 792, 795(e)	-	-	-	-	-	-	-	-	-	-	-	-	Ni—OH deformation (c), Si—O amorphous silica (e)
-	58.92**[a], 22.74-50.47**[b]	-	58.92*[e]	-	42.22*[f]	6.8-24.8**[g]	26.1-33.1**[g]	-		8.27	20.84	39.72	27.34	3.02	20.17	NiO wt.%
13.00**[a]	9.48**[a], 7.36-13.78**[b]	13.00*[e]	9.48*[e]	4.75*[f]	3.39*[f]	6.66-8.55**[g]	7.57-8.93**[g]	21.10**[h]		13.52***	15.13***	15.06***	10.5***	19.75***	15.46***	H_2O wt.%

(a) Baron and Petit (2016) and references therein, (b) Capitani and Ventruti (2018), (c) Frost et al. (2008), (d) Kloprogge et al. (1999), (e) Kloprogge et al. (2000) and references therein, (f) Ishida (1990), (g) Brindley et al. (1979), (h) Yeniyol (2014)

Table 6
FTIR absorption bands corresponding to the 500–1300 cm^{-1} region compared with Mg-Ni-phyllosilicates from the literature (* = weight percent calculated from the structural formula of the mineral analysed in the cited work, ** = weight percent presented in the cited work, *** = from the DTA-TG results in this study).

From literature									This study						
Lizardite	Népouite	Chrysotile	Pecoraite	Talc	Willemseite	Kerolite	Pimelite	Sepiolite	Garnierite	Type I	Type II	Type III	Type IV	Type Va	Type Vb	Assignment
-	-	-	900(c,e)	-	-	850-900(g)	850-900(g)	-	-	-	-	-	-	-	-	Si—O stretching (c,e), Si—O stretching of Si—OH groups (g)
-	-	955(c), 954-957(d,e)	-	-	-	-	-	-	-	968	968	968	-	-	-	Si—O stretching (c,d,e)
984(a)	984(a), 994(b)	-	-	-	-	-	-	982(h)	-	-	-	-	-	974	974	Si—O stretching (a,b, h)
-	-	-	1005(c,e)	-	-	-	-	-	-	-	-	-	-	-	-	Si—O stretching (c,e)
-	-	-	-	-	-	1014(g)	1014(g)	-	-	-	-	-	1000	-	-	Si-O vibration (g)
-	1024(a), 1020(c)	1020(c), 1018-1022(d,e)	1018(c)	1019(f)	-	-	-	1020(h)	1020(e)	-	-	-	-	-	-	Si—O stretching (a,c,d,e,h)
-	1040(c)	-	1027-1043(e)	1045(f)	1037(f)	-	-	-	1040(e)	1030	1030	1030	-	-	-	Si—O stretching (c,e)
1080(a)	1075, 1080(a), 1055(b)	1079-1085(c,e)	1068(c)	-	-	-	-	-	-	-	-	-	-	-	-	Si—O stretching (a,b,c), Si—O—Si stretching (c,e)
-	-	1102(d)	-	-	-	-	-	-	-	-	-	-	-	-	-	Si—O—Si stretching (d)
-	-	-	-	-	-	-	-	1208(h)	-	-	-	-	-	1210	1210	Si—O—Si stretching (h)
-	-	-	1225(c,e)	-	-	-	-	-	-	-	-	-	-	-	-	Si—O stretch in amorphous silica (c,e)
-	58.92**[a], 22.74-50.47**[b]	-	58.92*[e]	-	42.22*[f]	6.8-24.8**[g]	26.1-33.1**[g]	-		8.27	20.84	39.72	27.34	3.02	20.17	NiO wt.%
13.00**[a]	9.48**[a], 7.36-13.78**[b]	13.00*[e]	9.48*[e]	4.75*[f]	3.39*[f]	6.66-8.55**[g]	7.57-8.93**[g]	21.10**[h]		13.52***	15.13***	15.06***	10.5***	19.75***	15.46***	H_2O wt.%

(a) Baron and Petit (2016) and references therein, (b) Capitani and Ventruti (2018), (c) Frost et al. (2008), (d) Kloprogge et al. (1999), (e) Kloprogge et al. (2000) and references therein, (f) Ishida (1990), (g) Brindley et al. (1979), (h) Yeniyol (2014)

Table 7
FTIR absorption bands corresponding to OH-stretching zone compared with Mg-Ni-phyllosilicates from the literature (* = weight percent calculated from the structural formula of the mineral analysed in the cited work, ** = weight percent presented in the cited work, *** = from the DTA-TG results in this study).

From literature												This study						
Lizardite	Népouite	Chrysotile	Pecoraite	Talc	Willemseite	Kerolite	Pimelite	Synthetic Mg-talc	Synthetic Ni-talc	Sepiolite	Garnierite	Type I	Type II	Type III	Type IV	Type Va	Type Vb	Assignment
-	-	-	-	-	-	1600(g)	1600(g)	-	-	-	-	-	-	-	-	1660	1660	H_2O bending (g)
-	1635(c)	1635(c,d,e)	1632-1633(e)	-	-	-	-	-	-	-	1635(e)	1635	1635	1635	1635	-	-	H_2O O—H—O bend (c), Mg—OH stretching (d), absorbed H_2O bend (e)
-	-	-	-	-	-	-	-	-	-	-	1660, 1700(i)	-	-	-	-	1620	1620	Bound H_2O molecules
-	-	-	1674(c), 1674-1675(e)	-	-	-	-	-	-	-	-	-	-	-	-	-	-	H_2O O—H—O bending (c), H_2O OH-bending (e)
-	-	3300(c), 3000-3500(d)	3288(c)	-	-	-	-	-	-	-	-	-	-	-	-	-	-	H_2O OH stretching (c), Mg-OH stretching (d)
-	3400(b)	-	-	-	-	3400(g)	3400(g)	-	-	-	-	-	-	-	-	-	-	H_2O stretching (b,c), absorbed H_2O stretch (e,g)
-	3430(c)	-	3440(c,e)	-	-			3438(h)	3438(h)	3430(i)	3430(e)	-	-	-	-	-	-	H_2O OH stretching (c,e), OH stretching (g), weakly bound water (h), zeolitic H_2O (i)
-	-	-	-	-	-			-	-	3558(i)	-	-	-	-	-	3570	3570	OH stretching (g), OH stretching of bound H_2O (i)
-	3610(a,b)	-	-	-	-			-	-	-	-	-	-	-	-	-	-	OH stretching (a,g)
-	-	-	3630(c,e)	-	-			-	-	3622(i)	-	-	-	-	3625	3625	3625	OH stretching (e,g), H-O-H stretching of H_2O molecules weakly H-bonded to Si-O surface (i)
-	-	3643(d)	3645(c)	-	-	3400-3700(g)	3400-3700(g)	-	-	-	-	-	-	-	-	-	-	OH stretching (c,e,g), OH stretching of absorbed H_2O (d)
3648(a)	3644(a) 3646(b)	3651(c,e)	3650(c,e)	-	-			-	3627(h)	-	-	3645	3645	3645	-	-	-	OH stretching (a,b,c,e,g)
-	3672(c)	-	3683(c)	-	-			3677(h)	-	3688(i)	3672, 3685(e)	-	-	-	-	-	-	OH stretching (b,c,e,g)
-	-	3695(d)	-	-	-			-	-	-	-	-	-	-	-	-	-	OH bending of absorbed H_2O (d), OH stretching (g)
3698(a)	-	3697(c,e)	-	-	-			-	-	-	-	3685	3685	-	-	-	-	Mg—OH stretching (a), OH stretching (c,e,g)
-	58.92**	-	58.92**	-	46.45*	6.8-24.8**[g]	26.1-33.1**[g]	-	-	46.45*	-	8.27	20.84	39.72	27.34	3.02	20.17	NiO wt.%
13.00**	9.48**	13.00*	9.48**	4.75*	3.73*	6.66-8.55**[g]	7.57-8.93**[g]	4.75*	3.73*	21.10**		13.52***	15.13***	15.06***	10.5***	19.75***	15.46***	H_2O wt.%

(a) Baron and Petit (2016) and references therein, (b) Capitani and Ventruti (2018), (c) Frost et al. (2008), (d) Kloprogge et al. (1999), (e) Kloprogge et al. (2000) and references therein, (f) Ishida (1990), (g) Brindley et al. (1979), (h) Blanchard et al. (2018), (i) Yeniyol (2014)

(areas of few square micrometres or small powder samples), and may provide valuable information for a variety of industrial applications (e.g. Villanova-de-Benavent et al., 2012; Blanchard et al., 2018).

4. Conclusions

The detailed characterisation of Ni-phyllosilicates of the Falcondo Ni-laterites by means of DTA-TG, micro-Raman and IR spectroscopy leaded to the following conclusions:

1. Both the low oxide totals obtained by EMP and the large water loss at low temperatures of the talc-like garnierite confirm the presence of extra water in its structure, and therefore the use of the names "kerolite" and "pimelite" seem appropriate. Although these are also not accepted by the IMA-CNMMN, those terms have been widely used in the recent literature for Mg-Ni-bearing phyllosilicates with talc-like structures and additional water.
2. Despite the limited occurrence of Raman and FTIR spectra of Mg-Ni-phyllosilicates in the literature, each garnierite type described in this work is distinguishable by means of a characteristic Raman and FTIR pattern. Knowledge of characteristic Raman and FTIR vibrations of different garnierites with well constrained structure and composition is a significant improvement for the evaluation of the reliability of these techniques to characterise the mineral phases contained in the garnierites.
3. Certain Raman and FTIR bands can be related to serpentine group minerals, talc or sepiolite from the literature or from the analysed reference samples. From Raman spectra: a) the presence of serpentine is shown by the bands at ~230, ~340 and ~680 cm^{-1};; b) kerolite-pimelite particles were identified even when they were not detected by powder XRD; c) in garnierite mixtures, the band in the range 670–690 cm^{-1} is closer to 690 cm^{-1} in serpentine-dominated mixtures, whereas it is near 670 cm^{-1} in talc-dominated mixtures; and d) the band at ~195 cm^{-1} is exclusive of sepiolite. From FTIR: a) bands at 569, 606, 968 and 1030 cm^{-1} indicates the presence of serpentine group minerals; b) bands at 663, 712, 780 and 1000 cm^{-1} would indicate the presence of talc-like structures; and c) 640, 780, 974 and 1210 cm^{-1} are typical of sepiolite.
4. The variability of the position of bands in the 3625–3700 cm^{-1} range confirm the wide variety of Ni contents in the garnierites from the Falcondo mining district.

5. DTA-TG, Raman and FTIR spectroscopy results complement each other and provide a comprehensive picture of the form of water/OH contained in Ni-bearing Mg-phyllosilicates.

Acknowledgments

This research has been financially supported by FEDER Funds, the Spanish projects CGL2009-10924 and CGL2012-36263, and Catalan project 2014-SGR-1661 and a PhD grant to CVdB sponsored by the Ministerio de Educación (Spain). The help and hospitality extended by the staff at Falcondo Xstrata mine, especially Francisco Longo and Giovanni Bloise, are also gratefully acknowledged. Special thanks are to the donors of some of the samples used in this study: Dr. Alicja Lacinska from the British Geological Survey (LIZ-1 and LIZ-2), and Dr. Àngels Canals (TLC) and Dr. Esperança Tauler (SEP) from the Universitat de Barcelona. The technical support by Dr. Maite Garcia (DTA-TG, Universitat de Barcelona) and Elena Bailo (Raman spectroscopy map, WITEC) was indispensable for this work. Amaia Castellano-Calvo and Núria Pujol Solà are sincerely acknowledged for the additional Raman spectroscopy analyses. The Authors are very grateful to the three Reviewers (Dr. Emmanuel Fritsch and anonymous Reviewers) and to the Editor Prof. Emilio Galán for their fruitful and constructive comments, which improved the quality of the paper and ensured the accuracy of data interpretation.

References

Baron, F., Petit, S., 2016. Interpretation of the infrared spectra of the lizardite-népouite series in the near- and mid-infrared range. Am. Mineral. 101, 423–430.

Bian, Z., Li, Z., Ashok, J., Kawi, S., 2015. A highly active and stable Ni–Mg phyllosilicate nanotubular catalyst for ultrahigh temperature water-gas shift reaction. Chem. Commun. 51, 16324.

Blaha, J.J., Rosasco, G.J., 1978. Raman microprobe spectra of individual microcrystals and fibers of talc, tremolite, and related silicate minerals. Anal. Chem. 50, 892–896.

Blanchard, M., Méheut, M., Delon, L., Poirier, M., Micoud, P., Le Roux, C., Martin, F., 2018. Infrared spectroscopic study of the synthetic Mg-Ni talc series. Phys. Chem. Miner. 45, 843–854.

Bloise, A., Belluso, E., Fornero, E., Rinaudo, C., Barrese, E., Capella, S., 2010. Influence of synthesis conditions on growth of Ni-doped chrysotile. Microporous Mesoporous Mater. 132, 239–245.

Brindley, G.W., 1978. The structure and chemistry of hydrous nickel containing silicate and aluminate minerals. Bull. BRGM Sec. II 3, 233–245.

Brindley, G.W., Hang, P.T., 1973. The nature of garnierite: I. Structure, chemical compositions and color characteristics. Clay Clay Miner. 21, 27–40.

Brindley, G.W., Wan, H.M., 1975. Compositions, structures and thermal behaviour of nickel-containing minerals in the lizardite-népouite series. Am. Mineral. 60, 863–871.

Brindley, G.W., Bish, D.L., Wan, H.M., 1979. Compositions, structures, and properties of nickel-containing minerals in the kerolite-pimelite series. Am. Mineral. 64, 615–625.

Bunjaku, A., Kekkonen, M., Taskinen, P., Holappa, L., 2011. Thermal behaviour of hydrous nickel-magnesium silicates when heating up to 750 °C. Min. Process. Extract. Metal. 120, 139–146.

Caillère, S., 1965. Composition minéralogique des differents types de minerais de nickel de la Nouvelle-Calédonie. Mém. Muséum Nat. Hist. Natur. 12, 105–124.

Caillère, S., Hénin, S., 1957. VI. The mica minerals. In: Cameron Mackenzie, R. (Ed.), The Differential Thermal Investigation of Clays, Mineralogical Society of Great Britain, Clay Minerals group, London, pp. 176–187.

Caillère, S., Hénin, S., 1957. VIII.II. The serpentine and related minerals. In: Cameron Mackenzie, R. (Ed.), The Differential Thermal Investigation of Clays, Mineralogical Society of Great Britain, Clay Minerals group, London, pp. 220–230.

Caillère, S., Hénin, S., 1957. IX.I. The sepiolite minerals. In: Cameron Mackenzie, R. (Ed.), The Differential Thermal Investigation of Clays, Mineralogical Society of Great Britain, Clay Minerals group, London, pp. 231–239.

Capitani, G.C., Ventruti, G., 2018. Ni-serpentine nanoflakes in the garnierite ore from Campello Monti (Strona Valley, Italy): Népouite with some pecoraite outlines and the processing of Ni-containing ore bodies. Am. Mineral. 103, 629–644.

Cathelineau, M., Caumon, M.-C., Massei, F., Harlaux, M., Brie, D., 2014. A Raman Spectroscopy Study of the Ni-mg Kerolite Solid Solution: Sensitivity of the O-H Stretching Vibrations to Ni-mg Substitution, (11th GeoRaman Conf., 5030).

Cathelineau, M., Caumon, M.-C., Massei, F., Brie, D., Harlaux, M., 2015. Raman spectra of Ni-Mg kerolite: effect of Ni-Mg substitution on O-H stretching vibrations. J. Raman Spectrosc. 46, 933–940.

Cathelineau, M., Quesnel, B., Gautier, P., Boulvais, P., Couteau, C., Drouillet, M., 2016. Nickel dispersion and enrichment at the bottom of the regolith: formation of pimelite target-like ores in rock block joints (Koniambo Ni deposit, New Caledonia). Mineral. Deposita 101, 423–430.

Čermáková, Z., Hradil, D., Bezdička, P., Hradilová, J., 2017. New data on "kerolite-pimelite" series and the colouring agent of Szklary chrysoprase, Poland. Phys. Chem. Miner. 44, 193–202.

Dalvi, A.D., Gordon Bacon, W., Osborne, R.C., 2004. The past and the future of nickel laterites. In: Prospectors and Developers Association of Canada (PDAC) Int. Conv. pp. 1–27.

Dumas, A., Martin, F., Le Roux, C., Micoud, P., Petit, S., Ferrage, E., Brendlé, J., Grauby, O., Greenhill-Hooper, M., 2013. Phyllosilicates synthesis: a way of accessing edges contributions in NMR and FTIR spectroscopies. Example of synthetic talc. Phys. Chem. Miner. 40, 361–373.

Faust, G.T., 1966. The hydrous nickel-magnesium silicates – the garnierite group. Am. Mineral. 51, 33–36.

Freyssinet, Ph., Butt, C.R.M., Morris, R.C., 2005. Ore-forming processes related to lateritic weathering. Econ. Geol. 100th Anniv 681–722.

Fritsch, E., Juillot, F., Dublet, G., Fonteneau, L., Fandeur, D., Martin, E., Caner, L., Auzende, A.-L., Grauby, O., Beaufort, D., 2016. An alternative model for the formation of hydrous Mg/Ni layer silicates ("deweylite/garnierite") in faulted peridotites of New Caledonia: I. Texture and mineralogy of a paragenetic succession of silicate infillings. Eur. J. Mineral. 28, 295–311.

Frost, R.L., Ding, Z., 2003. Controlled rate thermal analysis and differential scanning calorimetry of sepiolites and palygorskites. Thermochim. Acta 397, 119–128.

Frost, R.L., Reddy, B.J., Dickfos, M.J., 2008. Raman spectroscopy of the nickel silicate mineral pecoraite – an analogue of chrysotile (asbestos). J. Raman Spectrosc. 39, 909–913.

Galí, S., Soler, J.M., Proenza, J.A., Lewis, J.F., Cama, J., Tauler, E., 2012. Ni-enrichment and stability of Al-free garnierite solid-solutions: a thermodynamic approach. Clay Clay Miner. 60, 121–135.

Golightly, J.P., 1981. Nickeliferous laterite deposits. Econ. Geol. 75th Anniv 710-735.

Golightly, J.P., 2010. Progress in understanding the evolution of nickel laterites. Econ. Geol. Spec. Pub. 15, 451–485.

Groppo, C., Rinaudo, C., Cairo, S., Gastaldi, D., Compagnoni, R., 2006. Micro-Raman spectroscopy for a quick and reliable identification of serpentine minerals from ultramafics. Eur. J. Mineral. 18, 319–329.

Guggenheim, S., Adams, J.M., Bain, D.C., Bergaya, F., Brigatti, M.F., Drits, V.A., Formoso, M.L.L., Galán, E., Kogure, T., Stanjek, H., 2006. Summary of recommendations of nomenclature committees relevant to clay mineralogy: report of the Association Internationale pour l'Étude des Argiles (AIPEA) nomenclature committee for 2006. Clay Clay Miner. 54, 761–772.

Hang, P.T., Brindley, G.W., 1973. The nature of garnierites – III. Thermal transformations. Clay Clay Miner. 21, 51–57.

Ishida, K., 1990. Identification of infrared OH librational bands of talc-willemseite solid solutions and Al(IV)-free amphiboles through deuteration. Mineral. J. 15, 93–104.

Jacobs, P.A., Nijs, H.H., Poncelet, G., 1980. Characterization of reduced natural garnierite and its catalytic activity for carbon monoxide hydrogenation. J. Catal. 64, 251–259.

Jones, B.F., Galán, E., 1988. Palygorskite–sepiolite. In: Bailey, S.W. (Ed.), Hydrous Phyllosilicates (Exclusive of Micas), Reviews in Mineralogy. vol. 19, Mineralogical Society of America, Chelsea, Michigan, pp. 631–674.

Kawi, S., Zao, Y.Z., 1999. Saponite catalysts with systematically varied Mg/Ni ratio: synthesis, characterization, and catalysis. Microporous Mesoporous Mater. 33, 49–59.

Kloprogge, J.T., Frost, R.L., Rintoul, L., 1999. Single crystal Raman microscopic study of the asbestos mineral chrysotile. Phys. Chem. Chem. Phys. 1, 2559–2564.

Kloprogge, J.T., Hammond, M., Frost, R.L., 2000. Low temperature synthesis and characterisation of pecoraite, a nickel containing phyllosilicate. Neues Jahrb. Mineral. Monatshefte 5, 193–206.

Kong, X., Zhu, Y., Zheng, H., Li, X., Zhu, Y., Li, Y.-W., 2015. Ni nanoparticles inlaid nickel phyllosilicate as a metal–acid bifunctional catalyst for low-temperature hydrogenolysis reactions. ACS Catal. 5, 5914–5920.

Krasilin, A.A., Gusarov, V.V., 2017. Redistribution of Mg and Ni cations in crystal lattice of conical nanotube with chrysotile structure. Nanosystems Phys. Chem. Math. 8, 620–627.

Lacinska, A.M., Styles, M.T., Bateman, K., Wagner, D., Hall, M.R., Gowing, C., Brown, P.D., 2016. Acid-dissolution of antigorite, chrysotile and lizardite for ex situ carbon capture and storage by mineralisation. Chem. Geol. 437, 153–169.

Linares, C.F., Acuña, G., Pérez, F., Ocanto, F., Corao, C., Betancourt, P., Brito, J.L., 2014. Garnierite: a new support for hydrodesulfurization catalysts. Mater. Lett. 131, 269–271.

McDonald, A., Scott, B., Villemure, G., 2009. Hydrothermal preparation of nanotubular particles of a 1:1 nickel phyllosilicate. Microporous Mesoporous Mater. 120, 263–266.

McKeown, D.A., Post, J.E., Etz, E.S., 2002. Vibrational analysis of palygorskite and sepiolite. Clay Clay Miner. 50, 667–680.

Nagata, H., Shimoda, S., Sudo, T., 1974. On dehydration of bound water of sepiolite. Clay Clay Miner. 22, 285–293.

Nelson, C.E., Iturralde-Vinent, M., Proenza, J.A., Draper, G., Escuder-Viruete, J., García-Casco, A., 2015. Tectonostratigraphic Map of the Greater Antilles (1:1,000,000 Scale): Recursos del Caribe, S.A..

Nickel, E.H., Nichols, M.C., 2009. Materials Data. In: http://www.materialsdata.com.

Petriglieri, J.R., Bersani, D., Salvioli-Mariani, E., Mantovani, L., Tribaudino, M., Lottici, P.P., Laporte-Magoni, C., 2014. Polymorphs of Serpentine Identification by Means of Raman Spectroscopy, (11th GeoRaman Conf., #5064).

Petriglieri, J.R., Salvioli-Mariani, E., Mantovani, L., Tribaudino, M., Lottici, P.P., Laporte-Magoni, C., Bersani, D., 2015. Micro-Raman mapping of the polymorphs of serpentine. J. Raman Spectrosc. 46, 953–958.

Rinaudo, C., Gastaldi, D., 2003. Characterization of chrysotile, antigorite and lizardite by FT-Raman spectroscopy. Can. Mineral. 41, 883–890.

Roqué-Rosell, J., Villanova-de-Benavent, C., Proenza, J.A., 2017. The accumulation of Ni in serpentines and garnierites from Falcondo Ni-laterite deposit (Dominican Republic) elucidated by means of μXAS. Geochim. Cosmochim. Acta 198, 48–69.

Rosasco, G.J., Blaha, J.J., 1980. Raman microprobe spectra and vibrational mode assignments of talc. Appl. Spectrosc. 34, 140–144.

Sivaiah, M.V., Petit, S., Beaufort, M.F., Eyidi, D., Barrault, J., Batiot-Dupeyrat, C., Valange, S., 2011. Nickel based catalysts derived from hydrothermally synthesized

1:1 and 2:1 phyllosilicates as precursors for carbon dioxide reforming of methane. Microporous Mesoporous Mater. 140, 69–80.

Springer, G., 1976. Falcondoite, Ni analogue of sepiolite. Can. Mineral. 14, 407–409.

Sufriadin, A.S., Idrus, A., Pramumijoyo, S., Warmada, I.W., Nur, I., Imai, A., Imran, A., Kaharuddin, M., 2012. Thermal and infrared studies of garnierite from the Soroako nickeliferous laterite deposit, Sulawesi, Indonesia. Indones. J. Geol. 7, 77–85.

Swinbourne, D.R., 2014. Modelling of nickel laterite smelting to ferronickel. In: High Temperature Processing Symposium. pp. 28–32.

Tauler, E., Proenza, J.A., Galí, S., Lewis, J.F., Labrador, M., García-Romero, E., Suárez, M., Longo, F., Bloise, G., 2009. Ni-sepiolite-falcondoite in garnierite mineralization from the Falcondo Ni-laterite deposit, Dominican Republic. Clay Miner. 44, 435–454.

Topsoe, H., Clausen, B.S., Massoth, F.E., 1996. Hydrotreating Catalysis. Springer, Berlin.

Villanova-de-Benavent, C., Aiglsperger, T., Jawhari, T., Proenza, J.A., Galí, S., 2012. Micro-Raman spectroscopy of garnierite minerals: a useful method for phase identification. Macla 16, 180–181.

Villanova-de-Benavent, C., Proenza, J.A., Galí, S., García-Casco, A., Tauler, E., Lewis, J.F., Longo, F., 2014. Garnierites and garnierites: Textures, mineralogy and geochemistry of garnierites in the Falcondo Ni-laterite deposit, Dominican Republic. Ore Geol. Rev. 58, 91–109.

Villanova-de-Benavent, C., Nieto, F., Viti, C., Proenza, J.A., Galí, S., Roqué-Rosell, J., 2016. Ni-phyllosilicates (garnierites) from the Falcondo Ni-laterite deposit (Dominican Republic): mineralogy, nanotextures and formation mechanisms by HRTEM and AEM. Am. Mineral. 101, 1460–1473.

Viti, C., 2010. Serpentine minerals discrimination by thermal analysis. Am. Mineral. 95, 631–638.

Wang, A., Freeman, J., Kuebler, K.E., 2002. Raman spectroscopic characterization of phyllosilicates. In: 33th Lun. Planet. Sci. Conf. vol. 1374.

Warner, A.E.M., Díaz, C.M., Dalvi, A.D., Mackey, P.J., Tarasov, A.V., 2006. World Nonferrous Smelter Survey, Part III: Nickel: Laterite. J.O.M. vol. 58, 11–20.

Wells, M.A., Ramanaidou, E.R., Verrall, M., Tessarolo, C., 2009. Mineralogy and crystal chemistry of "garnierites" in the Goro lateritic nickel deposit, New Caledonia. Eur. J. Mineral. 21, 467–483.

Yeniyol, M., 2014. Characterization of two forms of sepiolite and related Mg-rich clay minerals from Yenidoğan (Sivrihisar, Turkey). Clay Miner. 49, 91–108.